Acta Materialia 164 (2019) 530–546

Contents lists available at ScienceDirect

Acta Materialia

journal homepage: www.elsevier.com/locate/actamat

Full length article

Modelling recrystallization textures driven by intragranular fluctuations implemented in the viscoplastic self-consistent formulation

Miroslav Zecevic [a, b], Ricardo A. Lebensohn [b], Rodney J. McCabe [c], Marko Knezevic [a, *]

[a] Department of Mechanical Engineering, University of New Hampshire, Durham, NH, 03824, USA
[b] Theoretical Division, Los Alamos National Laboratory, Los Alamos, NM, 87544, USA
[c] Materials Science and Technology Division, Los Alamos National Laboratory, Los Alamos, NM, 87544, USA

ARTICLE INFO

Article history:
Received 27 July 2018
Received in revised form
29 October 2018
Accepted 1 November 2018
Available online 3 November 2018

Keywords:
Microstructures
Texture
Crystal plasticity
Recrystallization
Numerical algorithms

ABSTRACT

This paper presents a recrystallization model driven by intragranular orientation gradients and strain energy fields calculated by means of the viscoplastic self-consistent (VPSC) formulation. The VPSC model is extended for calculation of the coupling between intragranular stress fluctuations with corresponding second moments of lattice spin and misorientation fields in the grains. Access to these quantities allows modelling of transition bands and nucleation kinetics. In the proposed recrystallization model, grain growth is assumed to be proportional to the difference between the stored energy of each grain and that of the effective medium. Recrystallization textures for several cubic metals are simulated, showing good agreement with corresponding experiments. The model reveals the importance of considering appropriate, microstructurally-based and orientation-dependent recrystallization nucleation mechanisms. The recrystallization texture of heavily rolled copper with a strong cube texture component is found to be a consequence of nucleation at transition bands, which is also the cause of the recrystallization textures in compressed iron and drawn copper wire. In contrast, the recrystallization texture of rolled interstitial-free steel is found to be caused by grain boundary nucleation occurring in grains with the highest strain energy.

1. Introduction

Manufacturing processes of metallic components commonly consist of a sequence of shaping operations with intermediate anneals at appropriate temperatures [1,2]. During the annealing process, dislocation content, grain size and texture change due to recovery and recrystallization, which in turn affects the mechanical properties of the metallic component, and thus the material response during subsequent shaping operations. Therefore, understanding and predicting microstructural changes occurring during recrystallization of metallic material is of great practical importance.

Recrystallization nuclei are experimentally observed at deformation induced inhomogeneities such as grain boundaries, transition bands, shear bands, as well as second phase particles [1]. During grain boundary nucleation, a subgrain that has reached critical radius bulges out into the neighboring grain and becomes a nucleus [3]. The driving force for growth of the nuclei is the difference in energy stored during deformation between two sides of the moving boundary [4]. Hu, and Walter and Koch first observed formation of nuclei at transition bands [5,6], which are locations of high orientation gradient and thus stored energy as well [7]. Transition band nucleation has been investigated in detail in Refs. [8–11]. Shear band nucleation has also been observed in numerous studies [9,12–15]. However, details of the shear band nucleation mechanism are still unknown [1]. Considering the experimental observations of recrystallization, it is clear that the recrystallization process is greatly influenced by the deformed state of the polycrystal. Consequently, an accurate and physics-based recrystallization model should be informed by the measured or predicted deformed state. Since the output of the deformation model serves as an input for the recrystallization model, the complexity and performance of the recrystallization model are

* Corresponding author. University of New Hampshire, Department of Mechanical Engineering, 33 Academic Way, Kingsbury Hall, W119, Durham, NH, 03824, United States.
E-mail address: marko.knezevic@unh.edu (M. Knezevic).

https://doi.org/10.1016/j.actamat.2018.11.002
1359-6454/

determined by the available information provided by the deformation model. Spatially resolved full-field deformation models [16–22] can be coupled with full-field recrystallization models (e.g. Monte Carlo Potts models [23–27] or cellular automata models [28–30]). On the other hand, mean-field deformation models [31–35] can be accompanied by appropriate simpler recrystallization models. This paper formulates a recrystallization model based on the deformed state predicted by the mean-field viscoplastic self-consistent (VPSC) formulation [32].

A number of relatively simple recrystallization models initialized with microstructural quantities predicted by mean-field formulations have been proposed over the past several decades. Bunge and Köhler developed a model for predicting recrystallization textures based on deformation textures [36]. The orientations of the nuclei were chosen randomly and each nucleus was allowed to grow into the deformed matrix based on the misorientation between the nucleus and the matrix. Later, Engler proposed a recrystallization model in which the recrystallized orientation distribution function (ODF) was defined by superimposing the nucleation ODF and the growth ODF [37]. The nucleation ODF was artificially created based on experimental observations while the growth ODF was derived from the deformation texture. Kestens and Jonas developed a more sophisticated recrystallization model based on deformation texture and applied it to recrystallization of IF steels [38]. The nucleation probability of each orientation was related to its Taylor factor, which was assumed to be a measure representing the strain energy. Additionally, an oriented growth law based on the misorientation angle and misorientation axis between the nucleus and the matrix grains was employed. Hildenbrand et al. coupled the original VPSC model proposed by Molinari et al. [31] with the modified recrystallization model of Kestens and Jonas, and utilized the volume transfer scheme for texture evolution [39,40]. Along similar lines, Wenk et al. developed a deformation-based recrystallization model coupled with VPSC [32,41–43]. The nucleation was assumed to occur in the grains with the highest strain energy calculated based on the current values of the critical resolved shear stresses. Since in VPSC each grain is considered to be embedded in a homogenous effective medium, the growth rate was defined by the difference in strain energy between the grain and the effective medium having the averaged strain energy. Bolmaro et al. further improved the growth model by assuming pairing between grains and introducing a dependence of boundary mobility on misorientation angle [44]. Cram et al. coupled a simple polycrystal plasticity model proposed by Bouaziz and Buessler [45] with the nucleation model of Zurob et al. [46] and a mean-field growth model similar to the one of Wenk et al. [47]. Zurob et al.'s nucleation criterion, initially developed for static recrystallization, models formation of the nucleus at grain boundaries through subgrain growth [46]. When the growing subgrain reaches the critical radius, it bulges out into the neighboring grain and becomes a nucleus. A similar nucleation model was previously proposed by Humphreys [48]. In addition, the same type of nucleation model was later adopted by Han et al. within a cellular automata recrystallization approach coupled with crystal plasticity finite elements [49]. Sebald and Gottstein simulated evolution of recrystallization textures from the deformation textures using different nucleation mechanisms, namely: random nucleation, nucleation at shear bands and nucleation at preexisting nuclei [50]. An oriented growth model was employed with mobility defined based on the misorientation between the nucleus and deformed grain. The driving force for boundary migration was defined by the difference in strain energy, which was related to the grain's Taylor factor.

Most of the described mean-field recrystallization models are informed only with average grain orientations predicted by the associated deformation model. However, nucleation of recrystallization is influenced by intragranular orientation gradients developed during the deformation process [1]. In this regard, nucleation is often observed at transition bands, which form between portions of the grain deforming by different combinations of slip systems [5,6,11]. In the above summarized recrystallization models, magnitudes of intragranular orientation gradients were either completely neglected or directly related to other grain quantities (e.g. total accumulated shear within the grain or magnitude of the grain's strain rate). The orientation of the nucleus was assumed to be the same as the parent's orientation. This overly simplified treatment of intragranular orientation gradients within deformation and recrystallization models leads to poor predictions of recrystallization textures for recrystallization processes driven by intragranular orientation gradients.

In this paper we propose a recrystallization model that utilizes the intragranular misorientation distributions predicted by a recent extension of the VPSC model [51–53]. The model is computationally efficient, despite requiring calculation of the second-order moments of stress in the grains as deformation accumulates. Intragranular orientation gradients are calculated using intragranular misorientation distributions, and grains with transition bands are identified based on the shapes of the intragranular misorientation distributions. Orientations of the nuclei are appropriately chosen from the transition bands. Nucleation at grain boundaries is also considered. The proposed recrystallization model relies on the grain growth model proposed by Wenk et al. [41]. Recrystallization textures of face-centered cubic (fcc) and body-centered cubic (bcc) materials are simulated and reasonable agreement with experimental measurements is observed. Identification of grains developing transition bands is found to be critical for nucleation kinetics ensuring accurate predictions of recrystallization textures.

2. Model

First, we briefly summarize the standard VPSC model [32,54] and the recently developed algorithm for calculation of intragranular misorientation distributions [51,52] and grain fragmentation (GF) [53] within the VPSC formulation. This extended VPSC model has been designated as GF-VPSC [53]. Later, we provide a detailed description of the proposed recrystallization model, added to GF-VPSC.

2.1. VPSC model incorporating the calculation of intragranular misorientation distributions

A polycrystal is represented by a discrete set of ellipsoidal grains of a certain volume. The mean crystal orientation of each grain (r) is described by an active rotation quaternion, $\overline{\mathbf{q}}^{(r)}$, which brings the sample frame into alignment with the crystal frame. The crystal orientation varies spatially within the grain and, at a material point $\mathbf{x}$, can be described by the vector part of the misorientation quaternion, $\delta\mathbf{r}(\mathbf{x})$, defined with respect to the mean crystal orientation, $\overline{\mathbf{q}}^{(r)}$. Slip resistance of each slip system (s) is assumed to be spatially constant within each grain (r) and given by the mean grain value, $\tau_c^{s,(r)}$. The constitutive response at grain material point $\mathbf{x}$ is given by the viscoplastic equation:

$$\dot{\boldsymbol{\varepsilon}}(\mathbf{x}) = \dot{\gamma}_0 \sum_s \left(\frac{|\boldsymbol{\sigma}(\mathbf{x}) : \mathbf{m}^s(\mathbf{x})|}{\tau_c^{s,(r)}} \right)^n \operatorname{sign}(\boldsymbol{\sigma}(\mathbf{x}) : \mathbf{m}^s(\mathbf{x})) \mathbf{m}^s(\mathbf{x}), \qquad (1)$$

where $\dot{\gamma}_0$ is the reference shear rate, n is the inverse of rate sensitivity (set to 10 in all the simulations that follow) and $\mathbf{m}^s$ is the symmetric part of the Schmid tensor of slip system (s) in grain (r).

Under boundary conditions applied to a viscoplastic polycrystal, the mean stress and strain rate within each crystal and the homogenized macroscopic properties can be obtained through self-consistent homogenization [32]. The constitutive response at each material point $\mathbf{x}$ is approximated to be spatially constant within the grains, and described by a first-order Taylor expansion relating the mean values of the strain rate and stress in the grains [55]:

$$\dot{\boldsymbol{\varepsilon}}^{(r)} = \mathbf{M}^{(r)} : \boldsymbol{\sigma}^{(r)} + \dot{\boldsymbol{\varepsilon}}^{0(r)}, \tag{2}$$

where $\mathbf{M}^{(r)}$ and $\dot{\boldsymbol{\varepsilon}}^{0(r)}$ are compliance and back extrapolated strain rate of grain r. Each linearized grain is assumed to be an ellipsoidal inhomogeneity within an infinite matrix with the macroscopic properties, to which boundary conditions are applied. The stress and strain rate within the inhomogeneity are calculated using the equivalent inclusion approach [56], and the following interaction equation can be derived [32]:

$$\tilde{\dot{\boldsymbol{\varepsilon}}}^{(r)} = -\tilde{\mathbf{M}} : \tilde{\boldsymbol{\sigma}}^{(r)}, \tag{3}$$

where $\tilde{\dot{\boldsymbol{\varepsilon}}}^{(r)}$ and $\tilde{\boldsymbol{\sigma}}^{(r)}$ are deviations of the average strain rate and stress in the grains from the corresponding macroscopic values, and $\tilde{\mathbf{M}} = (\mathbf{I} - \mathbf{S})^{-1} : \mathbf{S} : \overline{\mathbf{M}}$ is the interaction tensor, which is a function of the symmetric Eshelby tensor, $\mathbf{S}$, and macroscopic compliance, $\overline{\mathbf{M}}$.

After each deformation step, the lattice rotation rate, velocity gradient and slip resistance rate are multiplied with the time increment, Δt, in order to produce the corresponding increments which are then utilized for explicit updating of the crystal orientation, grain shape and slip resistance, respectively. The slip resistance rate is given by Ref. [42]:

$$\dot{\tau}_c^{s,(r)} = \sum_{s'} h^{ss'} \dot{\gamma}^{s',(r)}, \tag{4}$$

where $h^{ss'}$ is a micro-hardening matrix. In this study, values of the micro-hardening matrix are set to $h^{ss'} = 1.0$, resulting in linear isotropic hardening. The initial slip resistance, τ_0^s, is set to unity.

Under the affine linearization (see Eq. (2)), VPSC only requires evaluation of the average stress and strain-rate in the grains, and thus intragranular spatial variations of orientation have no influence on the results. However, average fluctuations of intragranular quantities, starting from the second moments of the stress field in the grains, can still be calculated after each deformation step using the algorithms described below. In addition, Castelnau et al. [57] have used intragranular field fluctuations to improve the hardening model deriving an expression for slip resistance rate in function of both first and second moments of shear rates. Consequently, under this hardening model, field fluctuations also affect the strain energy within grains and, in turn, should also influence both nucleation and growth. Extension of Castelnau et al.'s fluctuation-based hardening model to recrystallization will be the subject of future work.

We consider two sources of intragranular stress fluctuations: variation of mean grain properties within the polycrystal [58–60] and intragranular spatial variation of orientation [53]. Both of these stress fluctuations are purely intragranular and they determine the stress variation inside of each grain. Since orientation and slip resistance completely determine the behavior of the grain within the polycrystal, grains with the same orientation and slip resistance will develop identical fluctuations. In what follows, we represent the symmetric second rank tensors in vector form so that matrix algebra can be used. The second moment of intragranular stress fluctuations is given by Refs. [54,59,61]:

$$\left\langle \delta\boldsymbol{\sigma}^{(\bar{q})} \otimes \delta\boldsymbol{\sigma}^{(\bar{q})} \right\rangle^{(r)} = \frac{2}{w^{(r)}} \frac{\partial \tilde{U}_T}{\partial \mathbf{M}^{(r)}} - \boldsymbol{\sigma}^{(r)} \otimes \boldsymbol{\sigma}^{(r)}, \tag{5}$$

where $\delta\boldsymbol{\sigma}^{(\bar{q})}$ is the fluctuation of stress with respect to the average grain stress for a grain with homogenous crystal orientation, $w^{(r)}$ is the grain volume fraction, $\tilde{U}_T$ is the effective stress potential and $\mathbf{M}^{(r)}$ is the grain compliance. The intragranular stress fluctuations due to the spatial variation of orientation within the grain are assumed to be linearly proportional to the misorientation vectors, where the linear transformation is defined by the derivative of stress with respect to the misorientation vector, $\left.\frac{\partial \boldsymbol{\sigma}}{\partial \delta \mathbf{r}}\right|_{\boldsymbol{\sigma}^{(r)}, \bar{\mathbf{q}}^{(r)}}$ (Eq. (1)). The second moment of these stress fluctuations is then given by Ref. [53]:

$$\left\langle \delta\boldsymbol{\sigma}^{(\delta r)} \otimes \delta\boldsymbol{\sigma}^{(\delta r)} \right\rangle^{(r)} = \left.\frac{\partial \boldsymbol{\sigma}}{\partial \delta \mathbf{r}}\right|_{\boldsymbol{\sigma}^{(r)}, \bar{\mathbf{q}}^{(r)}} \langle \delta\mathbf{r} \otimes \delta\mathbf{r} \rangle^{(r)} \left(\left.\frac{\partial \boldsymbol{\sigma}}{\partial \delta \mathbf{r}}\right|_{\boldsymbol{\sigma}^{(r)}, \bar{\mathbf{q}}^{(r)}} \right)^T, \tag{6}$$

where $\delta\boldsymbol{\sigma}^{(\delta r)}$ is the fluctuation of stress with respect to the average grain stress caused by the orientation fluctuation within the grain. The second moment of total intragranular stress fluctuations is obtained by superimposing the two intragranular stress distributions defined by Eqs. (5) and (6):

$$\langle \delta\boldsymbol{\sigma} \otimes \delta\boldsymbol{\sigma} \rangle^{(r)} = \left\langle \delta\boldsymbol{\sigma}^{(\bar{q})} \otimes \delta\boldsymbol{\sigma}^{(\bar{q})} \right\rangle^{(r)} + \left\langle \delta\boldsymbol{\sigma}^{(\delta r)} \otimes \delta\boldsymbol{\sigma}^{(\delta r)} \right\rangle^{(r)} +$$

$$\langle \delta\boldsymbol{\sigma} \otimes \delta\boldsymbol{\sigma} \rangle^{(r)} = \left\langle \delta\boldsymbol{\sigma}^{(\bar{q})} \otimes \delta\boldsymbol{\sigma}^{(\bar{q})} \right\rangle^{(r)} + \left\langle \delta\boldsymbol{\sigma}^{(\delta r)} \otimes \delta\boldsymbol{\sigma}^{(\delta r)} \right\rangle^{(r)} + \left\langle \delta\boldsymbol{\sigma}^{(\bar{q})} \otimes \delta\boldsymbol{\sigma}^{(\delta r)} \right\rangle^{(r)} + \left\langle \delta\boldsymbol{\sigma}^{(\delta r)} \otimes \delta\boldsymbol{\sigma}^{(\bar{q})} \right\rangle^{(r)}. \tag{7}$$

The cross-covariance terms (3rd and 4th terms on the right-hand side) define the covariance between the two stress fluctuation distributions.

Intragranular fluctuations of lattice rotation rate are assumed to be linearly proportional to the stress fluctuations and the intragranular misorientation vectors [51–53]. Consequently, an expression for the second moment of intragranular fluctuations of lattice rotation rate can be derived in terms of the second moment of stress fluctuations, $\langle \delta\boldsymbol{\sigma} \otimes \delta\boldsymbol{\sigma} \rangle^{(r)}$, and the second moment of misorientation vectors, $\langle \delta\mathbf{r} \otimes \delta\mathbf{r} \rangle^{(r)}$. Finally, the second moment of misorientation increment is calculated by integrating the

intragranular fluctuations of lattice rotation rate and is utilized for updating of the second moment of misorientation vectors for the next time increment. If the intragranular misorientation spread reaches a critical value, the fragmentation model subdivides the grain into two child grains, which then continue to evolve separately. Fragmentation takes place in orientation space by division of the grain's intragranular orientation distribution into two new distributions, which are assigned to fragments. Therefore, the total volume of the grain is divided into two fragments based on the orientation of each crystallite. Each fragment thus groups all crystallites that have a given orientation. The fragment does not represent a clustered set of single crystal material points in physical space separated by a high angle boundary from the remaining part of the grain, but a set of crystallites whose orientations are clustered in orientation space. The model is thus not capable of predicting grain subdivision in physical space, which happens by formation of new high angle boundaries. These aspects will be studied in future research. Due to fragmentation, certain grains from the initial texture will be represented by multiple fragments during deformation. In the recrystallization model, each such grain will be treated as a single grain whose state is defined by averaging its fragments' states.

2.2. Recrystallization model

During recrystallization new defect-free grains nucleate and grow into the deformed microstructure [1,62]. The nucleation process is heterogeneous and occurs at locations of high strain energy and high orientation gradient [1,63]. Growth of a recrystallized grain from a nucleus happens through high-angle boundary migration driven by the difference in strain energy between the two sides of the mobile boundary. Therefore, intragranular orientation gradients and strain energy determine the favorable places for nucleation and govern the subsequent boundary migration process. Consequently, in order to accurately predict recrystallization, intragranular orientation gradients and the strain energy of the microstructure need to be calculated first. Next, the nucleation and growth rules are developed based on these quantities.

2.2.1. Intragranular orientation gradients

In what follows, we consider a grain with orientation spread. The orientation at each material point, $\mathbf{x}$, of the grain is described with respect to the mean orientation of the grain, $\overline{\mathbf{q}}^{(r)}$, by the misorientation vector, $\delta\mathbf{r}(\mathbf{x})$. The spatial variation of orientation described by $\delta\mathbf{r}(\mathbf{x})$ is unknown. The only available information is the first and second moments of the misorientation vectors within the grain, $\delta\mathbf{r}^{(r)}$ and $\langle\delta\mathbf{r}\otimes\delta\mathbf{r}\rangle^{(r)}$, calculated with the deformation model. In what follows, we derive an expression for average intragranular orientation gradients as a function of the second moment $\langle\delta\mathbf{r}\otimes\delta\mathbf{r}\rangle^{(r)}$.

Let us consider one reference material point within the grain with an associated orientation described by a misorientation vector $\delta\mathbf{r}^{ref}$ (Fig. 1a). Next, let us assume that a spatially neighboring material point to the reference point has an unknown orientation defined by a misorientation vector $\delta\mathbf{r}$ (Fig. 1a). The misorientation between these two neighboring points can be approximated as: $\delta\mathbf{r}^{loc} \approx \delta\mathbf{r} - \delta\mathbf{r}^{ref}$. The vector $\delta\mathbf{r}^{loc}$ is a local neighbor misorientation vector that describes the misorientation between two spatially neighboring points within the grain, unlike the misorientation vectors $\delta\mathbf{r}^{ref}$ and $\delta\mathbf{r}$ which describe the misorientation between the orientation at particular point within the grain and the mean orientation of the grain, which is evident from Fig. 1a. Let us assume that the orientation of the spatially neighboring point to the reference point defined by $\delta\mathbf{r}$ can take any value from the grain's orientation spread and let us calculate the first and second moments of $\delta\mathbf{r}^{loc}$:

$$\left\langle \delta\mathbf{r}^{loc} \right\rangle^{(r),ref} = \left\langle \delta\mathbf{r} - \delta\mathbf{r}^{ref} \right\rangle^{(r),ref} = -\delta\mathbf{r}^{ref}, \tag{8}$$

$$\begin{aligned} \left\langle \delta\mathbf{r}^{loc} \otimes \delta\mathbf{r}^{loc} \right\rangle^{(r),ref} &= \left\langle \left(\delta\mathbf{r} - \delta\mathbf{r}^{ref}\right) \otimes \left(\delta\mathbf{r} - \delta\mathbf{r}^{ref}\right) \right\rangle^{(r),ref} \\ &= \delta\mathbf{r}^{ref} \otimes \delta\mathbf{r}^{ref} + \langle\delta\mathbf{r}\otimes\delta\mathbf{r}\rangle^{(r)}. \end{aligned} \tag{9}$$

The superscript *ref* emphasizes that these quantities are defined for one reference grain material point with orientation described by $\delta\mathbf{r}^{ref}$. The first and second moments of $\delta\mathbf{r}^{loc}$ define a distribution of all possible local neighbor misorientation vectors in grain r for one intragranular orientation described by $\delta\mathbf{r}^{ref}$. The distribution of possible local neighbor misorientations is assumed to be Gaussian with the probability density function (pdf) $f^{ref}(\delta\mathbf{r}^{loc})$ and illustrated by an iso-density ellipsoid in Fig. 1b.

Physically, the spatially neighboring points in the grain are more likely to have similar orientations. Consequently, the probability of finding smaller local neighbor misorientations $\delta\mathbf{r}^{loc}$ will be relatively higher in comparison to larger local neighbor misorientations. In order to take this spatial correlation of misorientations into account we introduce a Gaussian spatial correlation pdf, $g(\delta\mathbf{r}^{loc})$, which determines the likelihood of finding particular local neighbor misorientation only based on the spatial correlation criterion. The spatial correlation pdf $g(\delta\mathbf{r}^{loc})$ is assumed to be isotropic with zero mean and covariance matrix, $\mathbf{C} = \alpha\mathbf{I}$, where α is the variance and $\mathbf{I}$ is an identity matrix (Fig. 1b). Since $g(\delta\mathbf{r}^{loc})$ is isotropic, the misorientation axis has no effect and only the local misorientation angle determines the probability of finding that particular local neighbor misorientation. Variance α controls the magnitude of local neighbor misorientation angles. For small values of variance α, the probability of finding spatially neighboring points with large misorientation angle is very small. On the other hand, for large values of variance α, the probability of finding two neighboring orientations with a large misorientation angle would increase.

The spatial correlation pdf $g(\delta\mathbf{r}^{loc})$ describes the likelihood of finding a local neighbor misorientation $\delta\mathbf{r}^{loc}$ only based on the spatial correlation criterion, without taking into account available local neighbor misorientations defined by the pdf $f^{ref}(\delta\mathbf{r}^{loc})$. Consequently, for a given intragranular orientation described by $\delta\mathbf{r}^{ref}$ within the grain r with misorientation spread $\langle\delta\mathbf{r}\otimes\delta\mathbf{r}\rangle^{(r)}$, the spatially correlated likelihood of finding particular local neighbor misorientation $\delta\mathbf{r}^{loc}$ is described by the product of $f^{ref}(\delta\mathbf{r}^{loc})$ and $g(\delta\mathbf{r}^{loc})$ (Fig. 1c):

$$h^{ref}\left(\delta\mathbf{r}^{loc}\right) = \frac{f^{ref}\left(\delta\mathbf{r}^{loc}\right) g\left(\delta\mathbf{r}^{loc}\right)}{\int f^{ref}\left(\delta\mathbf{r}^{loc}\right) g\left(\delta\mathbf{r}^{loc}\right) d(\delta\mathbf{r})}. \tag{10}$$

Therefore, distribution $h^{ref}(\delta\mathbf{r}^{loc})$ is derived from the distribution of all possible local neighbor misorientations, $f^{ref}(\delta\mathbf{r}^{loc})$, by favoring the local neighbor misorientations with the smaller magnitude using the spatial correlation pdf $g(\delta\mathbf{r}^{loc})$. Since both $f^{ref}(\delta\mathbf{r}^{loc})$ and $g(\delta\mathbf{r}^{loc})$ are Gaussian pdfs, their product, $h^{ref}(\delta\mathbf{r}^{loc})$, is also Gaussian. Explicit expressions for the first and second moment of the product pdf $h^{ref}(\delta\mathbf{r}^{loc})$ can be derived in terms of the first and second moments of distributions $f^{ref}(\delta\mathbf{r}^{loc})$ and $g(\delta\mathbf{r}^{loc})$ [64]:

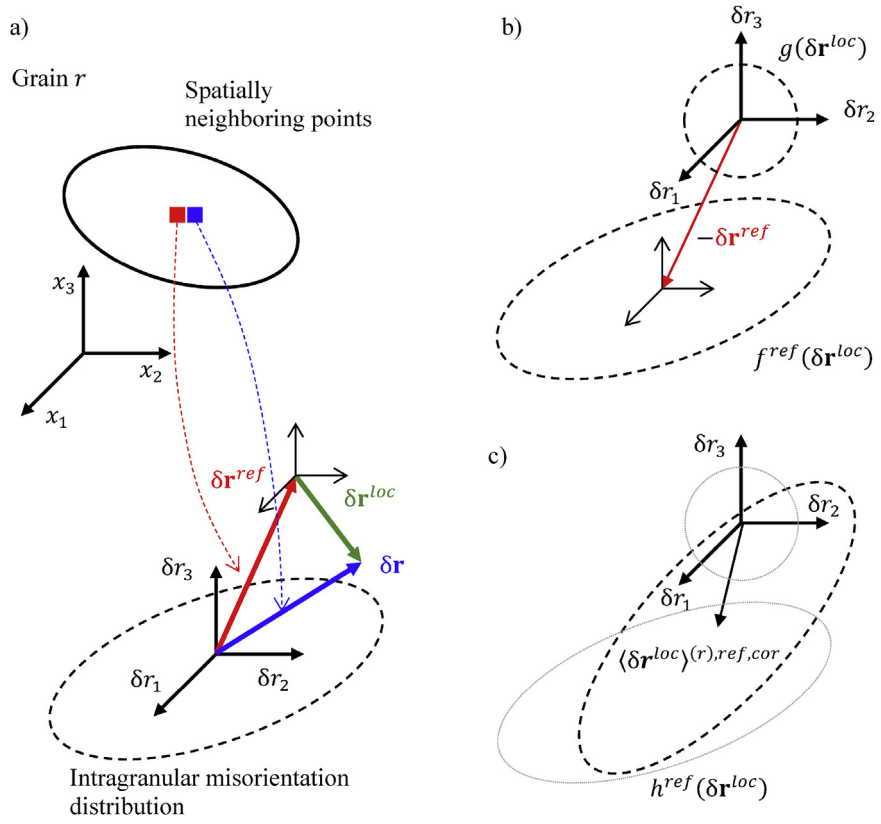

Fig. 1. (a) Illustration of local neighbor misorientation vector, $\delta\mathbf{r}^{loc}$, between the reference orientation, $\delta\mathbf{r}^{ref}$, and the spatially neighboring orientation, $\delta\mathbf{r}$; (b) iso-density ellipsoid of the distribution $f^{ref}(\delta\mathbf{r}^{loc})$ of all possible local neighbor misorientations for a given reference material point $\delta\mathbf{r}^{ref}$ and iso-density ellipsoid of the spatial correlation distribution $g(\delta\mathbf{r}^{loc})$; (c) local neighbor distribution $h^{ref}(\delta\mathbf{r}^{loc})$ obtained as product of $f^{ref}(\delta\mathbf{r}^{loc})$ and $g(\delta\mathbf{r}^{loc})$ for reference orientation $\delta\mathbf{r}^{ref}$.

$$\left\langle\delta\mathbf{r}^{loc}\right\rangle^{(r),ref,cor} = -\left(\langle\delta\mathbf{r}\otimes\delta\mathbf{r}\rangle^{(r)^{-1}} + \frac{1}{\alpha}\mathbf{I}\right)^{-1}\langle\delta\mathbf{r}\otimes\delta\mathbf{r}\rangle^{(r)^{-1}}\delta\mathbf{r}^{ref} \tag{11}$$

$$\left\langle\delta\mathbf{r}^{loc}\otimes\delta\mathbf{r}^{loc}\right\rangle^{(r),ref,cor} = \left\langle\delta\mathbf{r}^{loc}\right\rangle^{(r),ref,cor}\otimes\left\langle\delta\mathbf{r}^{loc}\right\rangle^{(r),ref,cor} + \left(\langle\delta\mathbf{r}\otimes\delta\mathbf{r}\rangle^{(r)^{-1}} + \frac{1}{\alpha}\mathbf{I}\right)^{-1}. \tag{12}$$

Distribution $h^{ref}(\delta\mathbf{r}^{loc})$, similar as distribution $f^{ref}(\delta\mathbf{r}^{loc})$, is defined for each intragranular orientation, $\delta\mathbf{r}^{ref}$, in the grain's orientation spread. Next, we define a distribution of all local neighbor misorientations for a grain by taking the volume average over $\delta\mathbf{r}^{ref}$ in Eqs. (11) and (12):

$$\left\langle\delta\mathbf{r}^{loc}\right\rangle^{(r)} = 0, \tag{13}$$

for one grain (described by Eqs. (13) and (14)) is derived by: (1) multiplying the pdf f^{ref} of all possible local neighbor misorientations for one material point with the spatial correlation pdf g and (2) averaging the resulting product pdf h^{ref} over all the material points within the grain. For $\alpha\to 0$, the second moment is $\langle\delta\mathbf{r}^{loc}\otimes\delta\mathbf{r}^{loc}\rangle^{(r)}\to 0$, and for $\alpha\to\infty$ we have $\langle\delta\mathbf{r}^{loc}\otimes\delta\mathbf{r}^{loc}\rangle^{(r)}\to 2\langle\delta\mathbf{r}\otimes\delta\mathbf{r}\rangle^{(r)}$. Consequently, for any given α, the second moment of local neighbor misorientations is bounded: $0 < \langle\delta\mathbf{r}^{loc}\otimes\delta\mathbf{r}^{loc}\rangle^{(r)} < 2\langle\delta\mathbf{r}\otimes\delta\mathbf{r}\rangle^{(r)}$. The variance α should be determined from experimental results or full-field simulations. However, for the purposes of the recrystallization model we are only interested in relative fluctuations of $\langle\delta\mathbf{r}^{loc}\otimes\delta\mathbf{r}^{loc}\rangle^{(r)}$ from grain to grain and not absolute magnitudes. Consequently, we assume $\alpha\to\infty$, which results in $\langle\delta\mathbf{r}^{loc}\otimes\delta\mathbf{r}^{loc}\rangle^{(r)} = 2\langle\delta\mathbf{r}\otimes\delta\mathbf{r}\rangle^{(r)}$. In this case the distribution of local neighbor misorientations corresponds to the distribution of all possible local neighbor misorientations defined by $f^{ref}\left(\delta\mathbf{r}^{loc}\right)$, averaged over all material points within the grain.

$$\left\langle\delta\mathbf{r}^{loc}\otimes\delta\mathbf{r}^{loc}\right\rangle^{(r)} = \left(\langle\delta\mathbf{r}\otimes\delta\mathbf{r}\rangle^{(r)^{-1}} + \frac{1}{\alpha}\mathbf{I}\right)^{-1}\langle\delta\mathbf{r}\otimes\delta\mathbf{r}\rangle^{(r)^{-T}}\left(\langle\delta\mathbf{r}\otimes\delta\mathbf{r}\rangle^{(r)^{-1}} + \frac{1}{\alpha}\mathbf{I}\right)^{-T} + \left(\langle\delta\mathbf{r}\otimes\delta\mathbf{r}\rangle^{(r)^{-1}} + \frac{1}{\alpha}\mathbf{I}\right)^{-1} \tag{14}$$

Therefore, the distribution of all local neighbor misorientations

For $\alpha\to\infty$, the distribution of local neighbor misorientations

defined by $\langle \delta \mathbf{r}^{loc} \rangle^{(r)}$ and $\langle \delta \mathbf{r}^{loc} \otimes \delta \mathbf{r}^{loc} \rangle^{(r)}$ can be viewed as an orientation difference distribution function (ODDF) calculated based on the grain's orientation distribution function (ODF) [65]. The ODDF is calculated by determining the orientation difference between each orientation in the ODF and all other orientations in the ODF. The ODDF provides statistical information on possible misorientations between neighboring points within the grain without considering the actual spatial configuration of the orientations within the grain [66].

The length of the local neighbor misorientation vector, $\left|\delta \mathbf{r}^{loc}\right|$, defines the local neighbor misorientation angle between spatially neighboring points, $\delta\theta$. Using the small angle approximation, the local neighbor misorientation angle, $\delta\theta$, can be written as:

$$\delta\theta \approx 2\left|\delta \mathbf{r}^{loc}\right|. \tag{15}$$

A distribution of magnitudes of three dimensional vectors with a Gaussian isotropic distribution is a Maxwell distribution [67,68]. Therefore, if we assume the distribution of local neighbor misorientation vectors, $\delta \mathbf{r}^{loc}$, is multivariate Gaussian and isotropic, the distribution of local neighbor misorientation angles $\delta\theta$ is the Maxwell distribution. In reality, the shape of the distribution of $\delta \mathbf{r}^{loc}$ will be anisotropic resulting in a distribution of local neighbor misorientation angles somewhat different from the Maxwell distribution. We note that Pantleon and Hansen [69] have shown that measured distributions of misorientation angles of geometrically necessary boundaries closely resemble the Maxwell and Rayleigh distributions [70]. The Rayleigh distribution describes distribution of magnitudes of two dimensional vectors with Gaussian isotropic distribution [68].

The average local neighbor misorientation angle is given by:

$$\langle \delta\theta \rangle^{(r)} \approx 2\left\langle \left|\delta \mathbf{r}^{loc}\right| \right\rangle^{(r)} = 2\left\langle \sqrt{\delta \mathbf{r}^{loc} \otimes \delta \mathbf{r}^{loc}} \right\rangle^{(r)} \approx 2\sqrt{2\mathbf{I} : \langle \delta \mathbf{r} \otimes \delta \mathbf{r} \rangle^{(r)}}. \tag{16}$$

The average local neighbor misorientation angle, $\langle \delta\theta \rangle^{(r)}$, represents an average measure of the misorientation angle between spatially neighboring points within the grain and it is thus related to the magnitude of the orientation gradient within the grain. If we assume that the distribution of local neighbor misorientation vectors, $\delta \mathbf{r}^{loc}$, is multivariate Gaussian, the distribution of the local neighbor misorientation angles, $\delta\theta$, follows a Maxwell-like distribution and the variance of the local neighbor misorientation angles, $\langle \delta\theta^2 \rangle^{(r)}$, is proportional to the mean value, $\langle \delta\theta \rangle^{(r)}$.

The orientation gradient can be calculated by dividing the local misorientation angle between the two spatially neighboring points, $\delta\theta$, with the distance, δx, between the two points: $\frac{\delta\theta}{\delta x}$. The distance δx depends on the grain size and in the present approach it is assumed to be the same for each grain, for simplicity. Consequently, the average magnitude of orientation gradient within the grain is directly proportional to the average local neighbor misorientation angle. In the recrystallization model, the average local neighbor misorientation angle is used as a measure of the orientation gradient.

2.2.2. Strain energy

The stored strain energy in a grain is approximated as [41,71,72]:

$$E^{(r)} = \rho^{(r)} \mu b^2 / 2, \tag{17}$$

where $\rho^{(r)}$ is the dislocation density within grain r, μ is the shear modulus and b is the Burgers vector. Since the increase of slip resistance due to work hardening is proportional to the square root of accumulated total dislocation density, $\sum_s (\tau_c^{s,(r)} - \tau_{c,0}^{s,(r)}) \sim \sqrt{\rho^{(r)}}$, the strain energy can be written as [41]:

$$E^{(r)} \sim \sum_s \left(\tau_c^{s,(r)} - \tau_{c,0}^{s,(r)}\right)^2. \tag{18}$$

Note that the total dislocation density is related only to the accumulated shear strain on slip systems within the grain. The calculated total dislocation density represents the sum of the statistically stored dislocation (SSD) density and the geometrically necessary dislocation (GND) density. Consequently, the GND density is also related only to the accumulated shear strain on slip systems and not to the intragranular gradients in strain or orientation. More accurate treatment would involve calculation of the GND density from the intragranular distributions of strain or orientation. On the other hand, the density of SSDs would evolve separately and the slip resistance would be calculated using the accumulated total dislocation density. In the current approach, we have chosen not to distinguish between the GND and SSD densities and to calculate their sum from the slip resistance which is the variable we evolve. The use of misorientation distributions—calculated using the procedure described earlier—for determination of GNDs, which in turn will affect the hardening and, consequently, the recrystallization behavior through the strain energy (Eq. (18)), will be the subject of future work.

2.2.3. Nucleation

Recrystallization nuclei form at heterogeneities in the deformed microstructure. Preferred nucleation sites in single phase alloys are grain boundaries, transition bands and shear bands [1]. High stored energy and orientation gradients at these locations promote subgrain growth during annealing [1,63]. In addition, presence of orientation gradients allows formation of high-angle boundaries during subgrain growth. The subgrain that reaches the size advantage becomes the nucleus. Nucleation events, both at grain boundaries and transition bands, are considered next.

2.2.3.1. Grain boundary nucleation. A high strain energy and orientation gradient at a grain boundary, caused by the strain incompatibilities [63], aid subgrain growth at grain boundary regions during recovery, preceding recrystallization. The subgrain that has gained a size advantage during recovery subsequently bulges out into the neighboring grain and becomes a nucleus. Presence of a high-angle grain boundary allows the nucleus to further grow into the neighboring grain. In the present model, the strain energy and local neighbor misorientation angle at the grain boundary are assumed to be proportional to the mean grain strain energy, $E^{(r)}$, and mean local neighbor misorientation angle, $\langle \delta\theta \rangle^{(r)}$, respectively. Consequently, it is implied that the variance of the intragranular strain energy and local neighbor misorientation angle distribution is proportional to the corresponding mean values. This assumption appears correct for the local neighbor misorientation angle, and an approximation for the strain energy. In what follows, mean grain values will be used for definition of grain boundary nucleation. Since the recrystallization model is mean-field, the actual spatial configuration of the polycrystal is not considered and each grain boundary is assumed to be a high angle boundary. Note that fragments are not treated as separate grains in the recrystallization model, but as parts of the parent grain. The fragment does not represent a part of the grain separated from the remainder of the grain by a high angle boundary. Therefore, it is assumed that a high angle grain boundary exists between the parent grains and not between the fragments.

A minimum strain energy and orientation gradient are necessary to initiate subgrain formation and growth preceding nucleation [1]. Consequently, in the model, only grains having reached a critical strain energy, E_{th}^{gb}, and critical local neighbor misorientation angle, $\delta\theta_{th}^{gb}$, are allowed to nucleate at a grain boundary.

Next, let us consider the nucleation probability of a grain with weight $w^{(r)}$ during time increment Δt. First, the grain boundary area is divided into a large number of area elements, dA, and time increment is divided into a large number of subincrements, dt. The probability that one nucleus forms during the subincrement dt in the boundary area dA is defined as [41]:

$$P_{gb}^{(r)}\left(dt, dA, E^{(r)}\right) = B_{gb}\exp\left(-\frac{A_{gb}}{E^{(r)2}}\right), \tag{19}$$

where A_{gb} is a constant determining the dependence of likelihood of grain boundary nucleation in terms of strain energy and B_{gb} is the pre-exponential factor that scales the probability ($B_{gb} \leq 1$). The constant A_{gb} is a function of grain boundary energy and temperature and, in the present model, is assumed to be a fitting parameter [41]. For simplicity, it is assumed that the increase of the local neighbor misorientation angle beyond the threshold value does not appreciably affect nucleation probability. The time increment dt and the area element dA are sufficiently small so that we may neglect the possibility of two or more nuclei forming. Therefore, there are only two possible outcomes of a nucleation event for dA during dt: success or failure. Consequently, one nucleation attempt represents a Bernoulli trial and the attempt nucleation probability $P_{gb}^{(r)}(dt\ , dA)$ is the success probability of a Bernoulli trial. The total time increment Δt is assumed sufficiently small so that the state of the grain does not change during Δt. In addition, the strain energy of a grain is assumed homogenous within the volume of the grain. Consequently, the probability of nucleation for each area element dA and subincrement dt is constant during total time increment Δt. Furthermore, outcome of each nucleation event is assumed to be independent of the outcomes of all the other nucleation attempts. Therefore, the nucleation of a grain with grain boundary area $A^{(r)}$ during time increment Δt represents a set of Bernoulli trials where each trial represents a nucleation attempt. The probability that at least one nucleus will form for a set of Bernoulli trials is given by:

$$\begin{aligned} P_{gb}^{(r)}\left(\Delta t, A^{(r)}, E^{(r)}\right) &= 1 - \binom{n}{0}\left(1 - P_{gb}^{(r)}\left(dt, dA, E^{(r)}\right)\right)^n \\ &= 1 - \left(1 - P_{gb}^{(r)}\left(dt, dA, E^{(r)}\right)\right)^n, \end{aligned} \tag{20}$$

where n represents the number of Bernoulli trials calculated as $n = \frac{\Delta t}{dt}\frac{A^{(r)}}{dA}$. The ratio of grain area to the area of element is approximated as $\frac{A^{(r)}}{dA} \approx \left(\frac{V^{(r)}/V_{tot}}{dV/V_{tot}}\right)^{2/3} = \left(\frac{w^{(r)}}{dw}\right)^{2/3}$, where dw represents the weight of the volume element dV, $V^{(r)}$ is the volume of the grain, V_{tot} is the total volume of the polycrystal and the power 2/3 is due to the square-cube law. Consequently, the final expression for the probability is:

$$P_{gb}^{(r)}\left(\Delta t, w^{(r)}, E^{(r)}\right) = 1 - \left(1 - B_{gb}\exp\left(-\frac{A_{gb}}{E^{(r)2}}\right)\right)^{\frac{\Delta t}{dt}\left(\frac{w^{(r)}}{dw}\right)^{2/3}}. \tag{21}$$

The time subincrement is set to $dt = 1.0$ of arbitrary time units, while the weight of the volume element is $dw = 10^{-6}$. The linearized expression for scaling of probability with time can be obtained by neglecting higher order terms in Eq. (21) [37]:

$$\begin{aligned} P_{gb}^{(r)}(\Delta t) = 1 - \Bigg(1 - \frac{\Delta t}{dt}P_{gb}^{(r)}(dt) \\ + \underbrace{\frac{\frac{\Delta t}{dt}\left(\frac{\Delta t}{dt} - 1\right)}{2}P_{gb}^{(r)}(dt)^2 - \ldots}_{\sim 0}\Bigg) \approx \frac{\Delta t}{dt}P_{gb}^{(r)}(dt) \end{aligned} \tag{22}$$

Note that as the time increment Δt increases, the number of Bernoulli trials n increases as well. Consequently, the probability of two or more successful Bernoulli trials during the Bernoulli process also increases. In the model, the time increment Δt is always set to a value resulting in the maximal nucleation probability less than 0.1, because in this case the probability of two or more successful Bernoulli trials is relatively small. Therefore, we can assume that if nucleation occurs, only one nucleus is formed.

At each time step, for each grain that has sufficiently high strain energy and local neighbor misorientation angle, the nucleation probability is calculated and compared to a random number 0–1. If the nucleation probability is higher than the random number, the grain nucleates a new dislocation-free grain with weight $w_{nuc} = 0.0001$. The strain energy of the newly formed grain is set to zero and slip resistance is set to the initial value adopted in the deformation model, before any strain hardening.

As was previously noted, a grain boundary nucleus develops from a grain boundary subgrain that has bulged out into a neighboring grain. Therefore, the orientation of the nucleated grain belongs to the set of grain boundary orientations. These orientations are substantially misoriented with respect to the mean grain orientation due to the different slip activity near the grain boundary [73,74]. Consequently, the orientations close to the grain boundary correspond to the tail of the grain's orientation spread. Fig. 2a shows a discrete representation of a grain's misorientation spread with the grain boundary misorientations, which are the potential nuclei misorientations, colored in red. The misorientations, $\delta\mathbf{r}^{gb}$, belonging to the grain boundary region satisfy the following condition: $\left|\delta\mathbf{r}^{gb}\right| > c \times SD(\delta\mathbf{r}^{gb}/\left|\delta\mathbf{r}^{gb}\right|)$, where c is a constant and $SD(\delta\mathbf{r}^{gb}/\left|\delta\mathbf{r}^{gb}\right|)$ is the standard deviation along the misorientation direction, $\delta\mathbf{r}^{gb}/\left|\delta\mathbf{r}^{gb}\right|$. The constant c determines the minimal misorientation angle between the mean grain orientation and grain boundary orientation. In conclusion, the orientation of the nucleus originating at the grain boundary is a randomly sampled grain boundary orientation (details are given in Appendix).

2.2.3.2. Transition band nucleation. During deformation, grains may subdivide into deformation bands which are regions that deform by different combinations of slip systems and thus develop large orientation gradients [75]. Transition bands are narrow regions between the deformation bands. The transition bands accommodate the orientation difference between the deformation bands and are thus places of large orientation gradient. The grains with well-developed transition bands have a multi-modal orientation distribution. Therefore, the modes of the orientation distribution correspond to the mean orientations of the deformation bands, while the orientations between the modes correspond to the transition band orientations. Nucleation during recrystallization is often observed in transition bands [11,76]. During recovery, a growing subgrain in a transition band quickly forms a high angle boundary due to presence of the high orientation gradient and becomes a nucleus. The orientation of the transition band nucleus

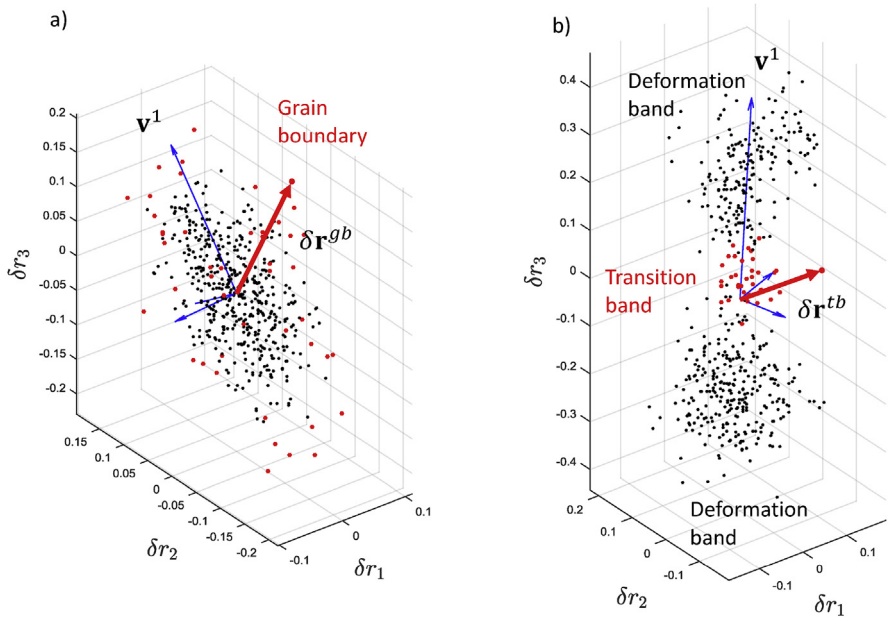

Fig. 2. Discrete representation of intragranular misorientation spread showing: a) misorientations corresponding to the points in the vicinity of the grain boundary (potential grain boundary nuclei orientations); b) misorientations corresponding to the transition band region of the bi-modal grain (potential transition band nuclei orientations). Dominant rotation axis vector, $\mathbf{v}^1$, defines the direction in which the distribution varies the most and corresponds to the largest eigenvector of the misorientation covariance matrix.

thus belongs to the set of transition band orientations.

In the present model, grains that have developed transition bands and orientations within transition bands can be identified based on the misorientation distribution [53]. If a grain has developed a bi-modal misorientation distribution, it is assumed that the transition band has formed within the grain and the orientations within the transition band are defined by the region between the modes of the misorientation distribution. Fig. 2b shows a discrete representation of the bi-modal misorientation distribution with the identified deformation and transition band misorientations. The projections of the transition band misorientations, $\delta\mathbf{r}^{tb}$, to the direction of dominant rotation axis, $\mathbf{v}^1$, are between the modes of the misorientation distribution. The dominant rotation axis represents the eigenvector corresponding to the largest eigenvalue of second moment $\langle\delta\mathbf{r}\otimes\delta\mathbf{r}\rangle^{(r)}$ [77]. Since the transition band nuclei evolve from the subgrains present at transition bands, the transition band orientations represent a set of possible nuclei orientations.

In the recrystallization model, only the grains with a bi-modal misorientation distribution are considered as possible transition band nucleation sites. In addition, the local orientation gradient and strain energy in the transition bands within those grains have to be larger than the threshold values. We assume that the local orientation gradient and the strain energy in the transition band are proportional to the average grain values, $\langle\delta\theta\rangle^{(r)}$ and $E^{(r)}$. Consequently, only grains with a bi-modal misorientation distribution, and a local neighbor misorientation angle and strain energy larger than the threshold values, $\delta\theta_{th}^{tb}$ and E_{th}^{tb}, are allowed to nucleate. The transition band nucleation probability is defined analogously to the grain boundary nucleation probability [41]:

$$P_{tb}^{(r)}\left(\Delta t, w^{(r)}, E^{(r)}\right) = 1 - \left(1 - B_{tb}\exp\left(-\frac{A_{tb}}{{E^{(r)}}^2}\right)\right)^{\frac{\Delta t}{dt}\left(\frac{w^{(r)}}{dw}\right)^{2/3}}, \qquad (23)$$

where A_{tb} is a constant determining the dependence of likelihood of transition band nucleation on strain energy and B_{tb} is the pre-exponential factor scaling the probability ($B_{tb} \leq 1$). Similar to grain boundary nucleation, it is assumed that the increase of average local neighbor misorientation angle above the threshold value does not affect the nucleation probability.

For each grain with a bi-modal misorientation distribution, the probability of nucleation at a transition band is calculated and compared to a random number 0–1. If the nucleation probability is larger than the random number, a new grain is nucleated in the same manner as for grain boundary nucleation. The orientation of the nucleus is randomly chosen from the transition band orientations (see Appendix).

2.2.4. Boundary migration

During annealing, high angle boundaries become mobile with boundary velocity given by:

$$v = MP, \qquad (24)$$

where M is the boundary mobility and P is the pressure acting on the boundary [1]. The driving pressure is caused by the difference in the stored energy between the two sides of the high angle boundary. Therefore, grains with lower strain energy grow while grains with higher strain energy shrink. We adopt a mean field approach and assume each grain is surrounded by the homogeneous effective medium [41,47]. The boundary velocity of each grain is thus proportional to the difference between the stored energy of the grain, $E^{(r)}$, and the stored energy of the effective medium, E^{avg} [41]:

$$v^{(r)} = M\left(E^{avg} - E^{(r)}\right), \qquad (25)$$

where the stored energy of the effective medium is the average for the polycrystal, $E^{avg} = \sum_r w^{(r)}E^{(r)}$. The change in grain weight due to boundary migration with velocity $v^{(r)}$ during time increment Δt is given by Ref. [41]:

$$w^{(r),t+\Delta t} = w^{(r),t} + 3M\left(\frac{4\pi}{3}\right)^{\frac{1}{3}}\left(w^{(r),t}\right)^{\frac{2}{3}}\left(E^{avg} - E^{(r)}\right)\Delta t. \quad (26)$$

After updating the weight of each grain, a normalization of grain weights is performed to ensure that $\sum_r w^{(r),t+\Delta t} = 1$.

2.2.5. Algorithm

Summarizing, the algorithm of the proposed recrystallization model is as follows:

Calculate the average local neighbor misorientation angle, $\langle\delta\theta\rangle^{(r)}$, and strain energy, $E^{(r)}$, for each grain after deformation. For each recrystallization time increment:

1) Calculate the average strain energy E^{avg}.
2) Grain boundary nucleation:
   For each grain r:
   if $E^{(r)} > E_{th}^{gb} \wedge \langle\delta\theta\rangle^{(r)} > \delta\theta_{th}^{gb}$:
   a) Calculate nucleation probability $P_{gb}^{(r)}\left(\Delta t, w^{(r)}, E^{(r)}\right)$
   b) Draw a random number $0 < rand < 1$
   c) **if** $rand < P_{gb}^{(r)}$:
   Create a new grain with zero strain energy, initial slip resistance and randomly sampled grain boundary orientation.
3) Transition band nucleation:
   For each bi-modal grain r:
   if $E^{(r)} > E_{th}^{tb} \wedge \langle\delta\theta\rangle^{(r)} > \delta\theta_{th}^{tb}$:
   a) Calculate nucleation probability $P_{tb}^{(r)}\left(\Delta t, w^{(r)}, E^{(r)}\right)$
   b) Draw a random number $0 < rand < 1$
   c) **if** $rand < P_{tb}^{(r)}$:
   Create a new grain with zero strain energy, initial slip resistance and randomly sampled transition band orientation.
4) Weight update:
   For each grain r update the weight:
   $w^{(r),t+\Delta t} = w^{(r),t} + 3M\left(\frac{4\pi}{3}\right)^{\frac{1}{3}}\left(w^{(r),t}\right)^{\frac{2}{3}}\left(E^{avg} - E^{(r)}\right)\Delta t.$
5) Renormalize the grain weights.

3. Results

We apply the developed model to several case studies of coupled deformation and static recrystallization modeling. The recrystallization model parameters are given in Table 1. The nucleation parameters are calibrated first based on experimental observations of the predominant nucleation mechanism. Adjusting the relative ratio of transition band and grain boundary nucleation parameters allows transitioning from a texture consisting of transition band orientations to a texture corresponding to the highest strain energy orientations. Next, mobility of grain boundaries is adjusted with the goal of achieving a balance between nucleation and growth. Increasing the mobility results in faster growth and thus a smaller number of grains at the end of recrystallization and vice versa. Dynamic recrystallization can be performed simply by calling the recrystallization model after each or several deformation steps [41,47].

3.1. Annealing of cold drawn copper wire

We simulate cold drawing of copper wire to 90% area reduction and subsequent annealing at 700 °C reported in Ref. [78]. The central region of the wire is subjected to uniaxial tension while regions closer to the surface of the wire undergo additional shearing [78]. The applied boundary conditions in the model correspond to the central region of the wire and the predictions are compared to the measurements taken at the central region. The initial texture of the sample is represented by 400 randomly oriented spherical grains, which is enough to accurately describe the effective response of the polycrystal and its evolution, and thus the homogeneous effective medium as well. Consequently, an increase in the number of grains would not change the behavior of the chosen 400 grains because the behavior of a grain is determined by its orientation and the effective medium. In addition, since the orientation of each grain is described by an orientation distribution, a smaller number of grains is necessary for accurate texture modeling in comparison to the classical mean-field models in which grain orientation is described only by one mean value. The grains are assumed to deform by $\{111\}\langle 1\bar{1}0\rangle$ slip and linear hardening given by Eq. (4).

Fig. 3a and c compare the measured deformation texture and the predicted deformation texture in the central region of the wire after 90% area reduction. The measured texture consists of major [111] (the intensity of 26.7) and minor [100] (the intensity of 7.6) components. The predicted intensity of the [001] component is considerably higher than the experimentally measured intensity. This discrepancy is attributed to the very slow evolution of intragranular misorientation spreads for grains close to [001] in simulations [51]. Consequently, the orientations are more clustered around the [001] resulting in the higher intensity. On the other hand, the predicted total fraction of orientations with tension directions within 15° of [001] is 0.4, while the orientations with tension directions within 15° of [111] total 0.6. These predictions for the fractions of [111] and [001] components are in very good agreement with [79,80], where for copper the ratio of [001] to [001]+[111] is estimated to be around 0.37.

After 90% drawing, the mean orientations of grains have clustered around the stable components and the intensity of the texture is predominantly determined by the magnitudes of the grain orientation spreads, which have also reached their stable

Table 1
Recrystallization model parameters.

		90% drawn copper	95% rolled copper	88% compressed iron	85% rolled IF steel
Grain boundary nucleation	E_{th}^{gb}	0.0	N/A	0.0	738.0
	$\delta\theta_{th}^{gb}$	0.0	N/A	0.14	0.0
	A_{gb}	3.759×10^{5}	N/A	1.114×10^{4}	4.142×10^{5}
	B_{gb}	1.783×10^{-6}	N/A	2.679×10^{-6}	2.932×10^{-6}
	c	2.0	N/A	2.0	1.0
Transition band nucleation	E_{th}^{tb}	0.0	0.0	132.0	N/A
	$\delta\theta_{th}^{gb}$	0.0	0.867	0.0	N/A
	A_{tb}	4.547×10^{4}	5.209×10^{5}	1.029×10^{3}	N/A
	B_{tb}	5.870×10^{-6}	3.058×10^{-6}	5.960×10^{-6}	N/A
Growth	M	3.0×10^{-9}	3.0×10^{-9}	1.7×10^{-8}	4×10^{-9}

states. On one hand, the orientation spreads of grains that have reached stable components tend to shrink because the stable regions are convergent and all orientations within them reorient toward the stable component. On the other hand, the stress fluctuations caused by the variation of grain properties within the polycrystal increase the orientation spreads. These two effects eventually balance each other and the orientation spreads of grains that have reached stable components stop evolving with further deformation. The stable spread magnitude determines the intensity of the stable components in the deformation texture. Therefore, because the model overpredicts the [001] intensity, we conclude that the model tends to under predict the magnitudes of orientation spreads for grains with a tension direction close to [001]. A possible reason is the absence of neighborhood effects on the grain's stress distribution in the GF-VPSC model. In an actual polycrystal, the intragranular stress distribution of each grain is affected by stress states of neighboring grains. During tension of fcc polycrystals, grains clustered around [001] will likely be surrounded by grains with tension direction close to [111] because the majority of the grains in the polycrystal are close to [111]. Since the stress state is predominantly determined by the grain's orientation, the [001] grains are likely to be surrounded by grains with quite different stress states. Consequently, the effect of the neighborhood on the grain's stress state will be fairly strong for [001] grains. On

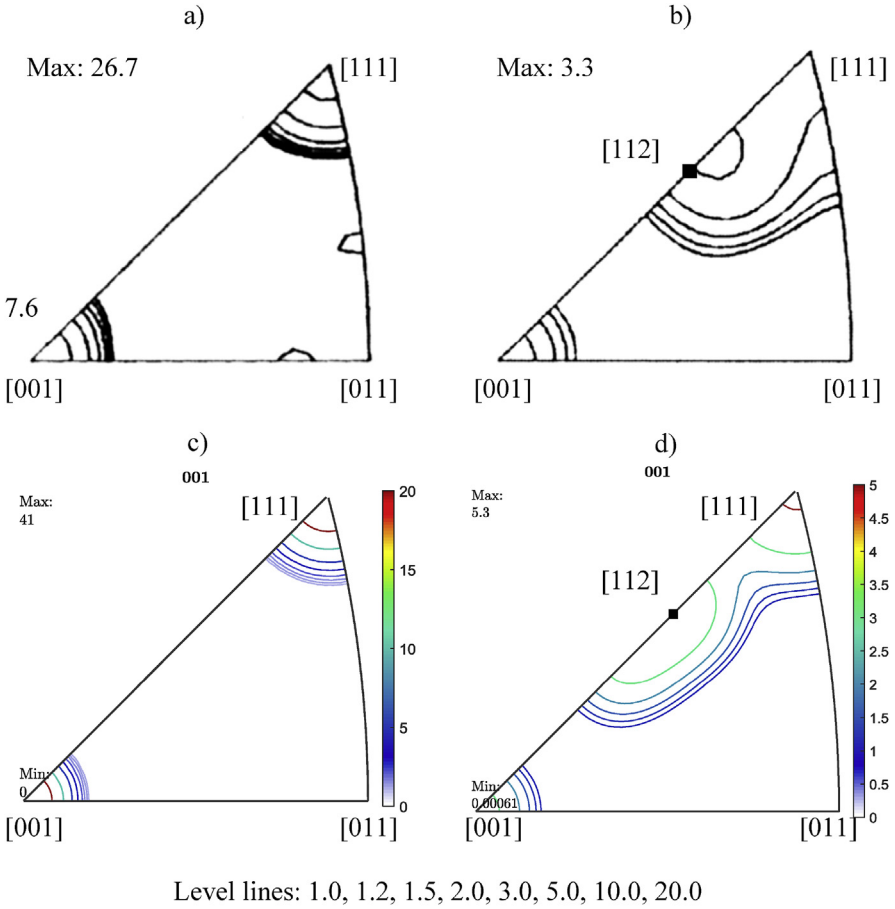

Fig. 3. Inverse pole figures showing deformation and recrystallization textures of 90% drawn copper wire: a) measured deformation texture at the central region of the wire; b) measured recrystallized texture at the central region of the wire; c) predicted deformation texture; d) predicted recrystallized texture.

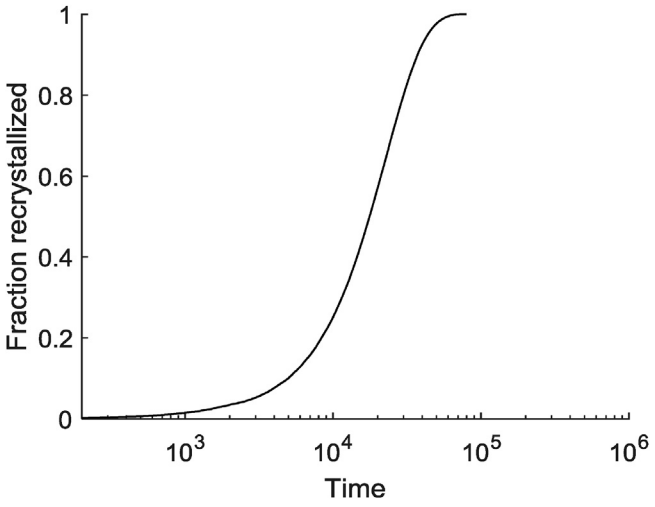

Fig. 4. Predicted evolution of the volume fraction of recrystallized material during recrystallization of 90% drawn copper wire.

the other hand, the [111] grains are likely surrounded by grains with similar orientation and thus similar stress state resulting in weaker effect of the neighborhood on the grain's stress distribution. The neighborhood effects are missing in the GF-VPSC model and the stress distribution of each grain is affected equally by all other grains in the polycrystal. The averaged effect of all other grains on the grain's stress distribution seems to be weaker than the actual effect of the local neighborhood for the grains in the [001] region. Consequently, the orientation spreads of grains with a tension direction close to [001] might be inaccurately predicted.

Fig. 3b and d compare the predicted and measured recrystallization textures. The experimental recrystallization texture was measured using electron backscatter diffraction (EBSD) at the central region of the 90% drawn wire after annealing at 700 °C for 1 h. The central region was not fully recrystallized and no extensive abnormal grain growth was observed. The experimental recrystallization texture consists of [001], [111] and [112] components. It is noted that the [112] component is not strong in the deformation texture. In the recrystallization model, the nucleation and growth constants were adjusted to favor nucleation at transition bands (Table 1) and the material was fully recrystallized. The model predicts well the [001], [111] and [112] components in the recrystallized texture. On one hand, [001] and [111] components are a result of the nucleation at grain boundaries within [001] and [111] grains in the deformed texture. The GF-VPSC model predicts transition band orientations clustered around [112], and thus the transition band nucleation is responsible for the [112] recrystallization texture component in the simulation. We note that the [112] component is practically absent from the predicted deformation textures in both the simulation and experiment, and only emerges after recrystallization. Similar behavior is observed in rolled fcc where a strong cube recrystallization component is observed after recrystallization, and not after deformation. We believe that the same transition band nucleation process is responsible for both of these phenomena [52].

Fig. 4 shows the evolution of recrystallized volume, X_V, as a function of time, $\log t$. The plot shows a characteristic sigmodal shape [1]. At the beginning of recrystallization, a typical incubation period is observed followed by an increased rate of recrystallization and a linear region. As the recrystallized volume increases, the impingement of newly formed grains occurs reducing the rate of recrystallization. In the model, the impingement of the defect free grains is captured through the reduction of the average strain energy of the effective medium due to the increase of recrystallized material, which results in a lower recrystallization rate.

3.2. Annealing of 95% rolled copper

Next, we simulated rolling of copper to 95% reduction and subsequent annealing [81]. The rolling process was modelled by imposing plane strain compression (PSC) boundary conditions. This approximation is valid for the central region of the rolled plate, away from the rolls. The initial texture of the sample is represented by 400 randomly oriented spherical grains deforming by $\{111\}\langle 1\bar{1}0\rangle$ slip and linear hardening (Eq. (4)).

The predicted and measured deformation textures are compared in Fig. 5a and c. The main components of the deformation texture are predicted well. However, the simulated texture is noticeably weaker than the measured one. The likely cause for discrepancy is the over prediction of intragranular orientation spreads of grains at stable regions.

Fig. 5b and d shows the predicted and measured recrystallization textures. The well-known cube recrystallization texture is observed both in the simulation and experiment. It is widely accepted that the cube recrystallization texture is caused by nucleation at transition bands with the cube orientation in the center of the band [9,11,76]. The model predicts that approximately 25% of the initial grains form transition bands at the end of deformation. Fig. 6 shows all transition band orientations (one orientation for each transition band) color-coded according to the average local neighbor misorientation angle. A majority of predicted crystallographic orientations of transition bands are concentrated around the cube orientation, in good agreement with experimental observations. In addition, the grains with cube-oriented transition bands possess the highest intragranular misorientation. The remaining transition band orientations are concentrated around the Goss, 45°ND rotated cube and $(011)[2\bar{1}\bar{1}]$ orientations. Dillamore and Katoh predicted that Goss is also likely to develop transition bands [76]. It is noted that at lower reductions (~80%), the model predicts predominantly cube-oriented transition bands. In the recrystallization simulation, only transition band nucleation is allowed and only the transition bands with the highest misorientation are allowed to nucleate (Table 1). The predicted cube recrystallization texture is thus directly caused by nucleation in cube-oriented transition bands, which possess the highest intragranular orientation gradient.

Fig. 7 shows the process of formation of cube transition bands during rolling of copper. Evolution of a grain with [010]||ND and a small initial orientation spread is considered in the $\Phi = 90°$ section of Euler space during rolling. The schematic on the left shows analysis by Dillamore and Katoh obtained using a Taylor iso-strain approach for calculation of reorientation tendencies in Euler space [1,76]. As the grain approaches the cube orientation along the [010]||ND line, portions of the orientation spread that are not on the [010]||ND line diverge by rotation around the RD, while the portion on the [010]||ND converges to the cube orientation. Therefore, the grain subdivides into two fragments and the transition band forms with the cube orientation in the center. The plot on the right shows evolution of the orientation spread of the grain with [010]||ND predicted by the GF-VPSC model. The orientation spread is represented by 500 discrete points and plotted for 7 strain levels and color-coded according to the strain level. The model predicts that the portions of the orientation spread away from the [010]||ND line quickly converge to different stable fibers, while the portion of the spread on the [010]||ND line reorients to the cube orientation and subsequently diverges by rotation around the RD as it approaches

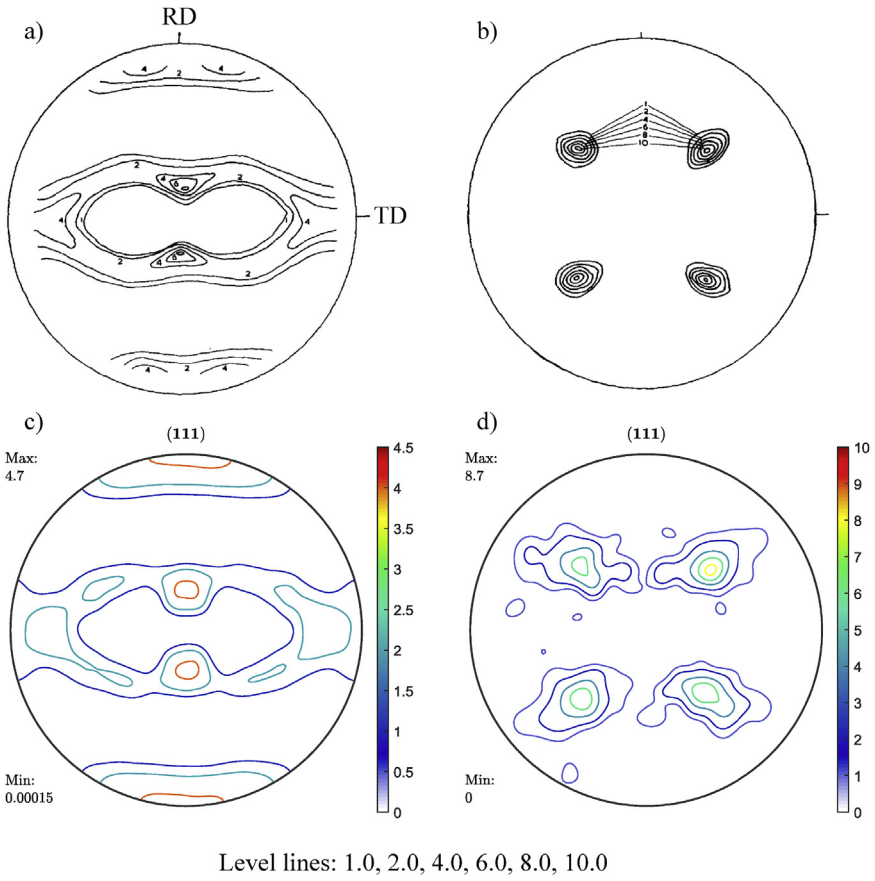

Fig. 5. {111} pole figures showing deformation and recrystallization textures of 95% rolled copper: a) measured deformation texture; b) measured recrystallized texture; c) predicted deformation texture; d) predicted recrystallized texture.

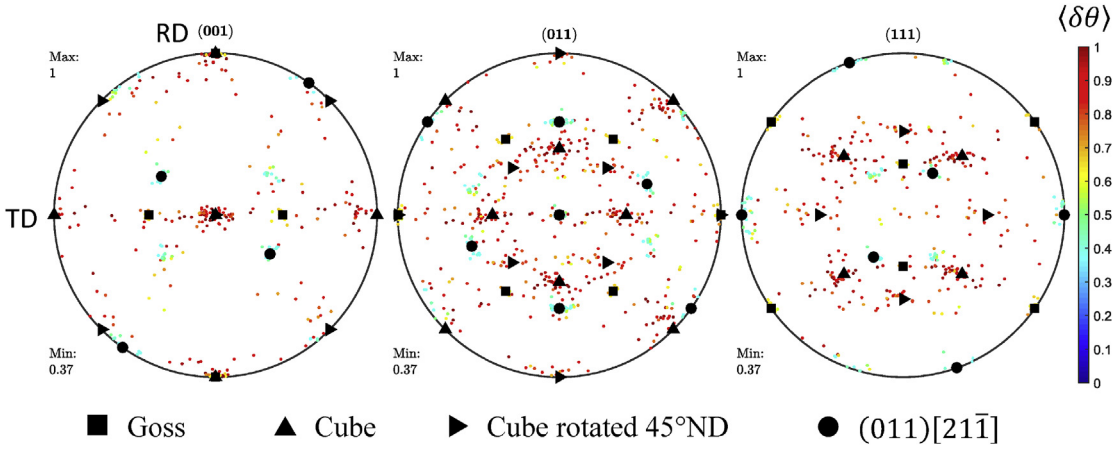

Fig. 6. Predicted transition band orientations (one orientation per transition band) after 95% plane strain compression of copper, color-coded according to the average local neighbor misorientation angle within the corresponding grain, $\langle\delta\theta\rangle^{(r)}$. (For interpretation of the references to color in this figure legend, the reader is referred to the Web version of this article.)

the cube. Therefore, the model predicts formation of the cube-oriented transition band in a similar manner as described by Dillamore and Katoh.

3.3. Annealing of 88% compressed iron-carbon alloy

Compression of Fe-0.02%C to 88% strain and subsequent annealing reported in Ref. [82] is simulated using GF-VPSC furnished with the recrystallization model. The initial texture is represented by 400 randomly oriented spherical grains deforming by {110}⟨111⟩ and {112}⟨111⟩ slip and linear hardening. Initial slip resistance and hardening are assumed to be the same for each mode (Eq. (4)).

Fig. 8a and c compare the predicted and measured deformation textures. The measured texture consists of a strong [111] component and a weaker [001] component. Similar texture is obtained

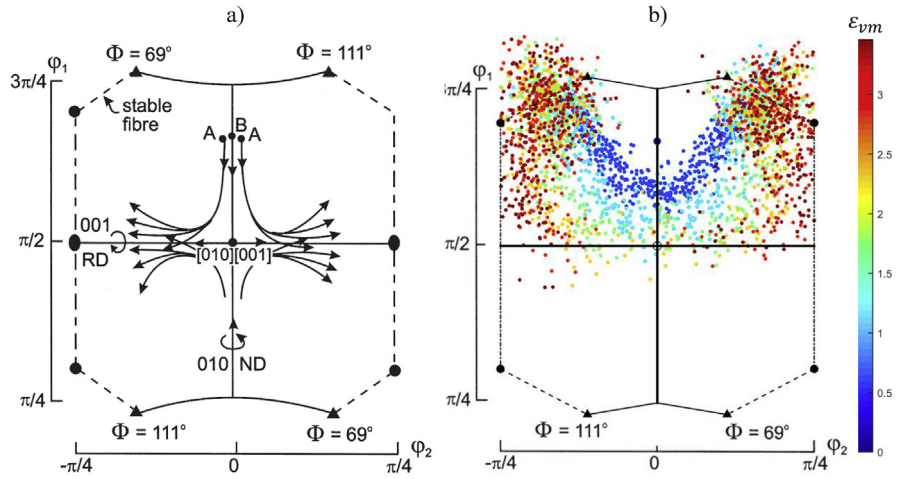

Fig. 7. Formation of the cube transition band during rolling of copper illustrated on the section $\Phi = 90°$ of Euler space; a) evolution of the orientation spread (A B A) of a grain with [010]||ND initial orientation (Dillamore and Katoh, 1974; Humphreys and Hatherly, 2004); b) predicted evolution of the orientation spread of a grain with [010]||ND initial orientation using GF-VPSC as a function of strain. The spread was represented by a set of discrete orientations and color-coded according to the strain level. (For interpretation of the references to color in this figure legend, the reader is referred to the Web version of this article.)

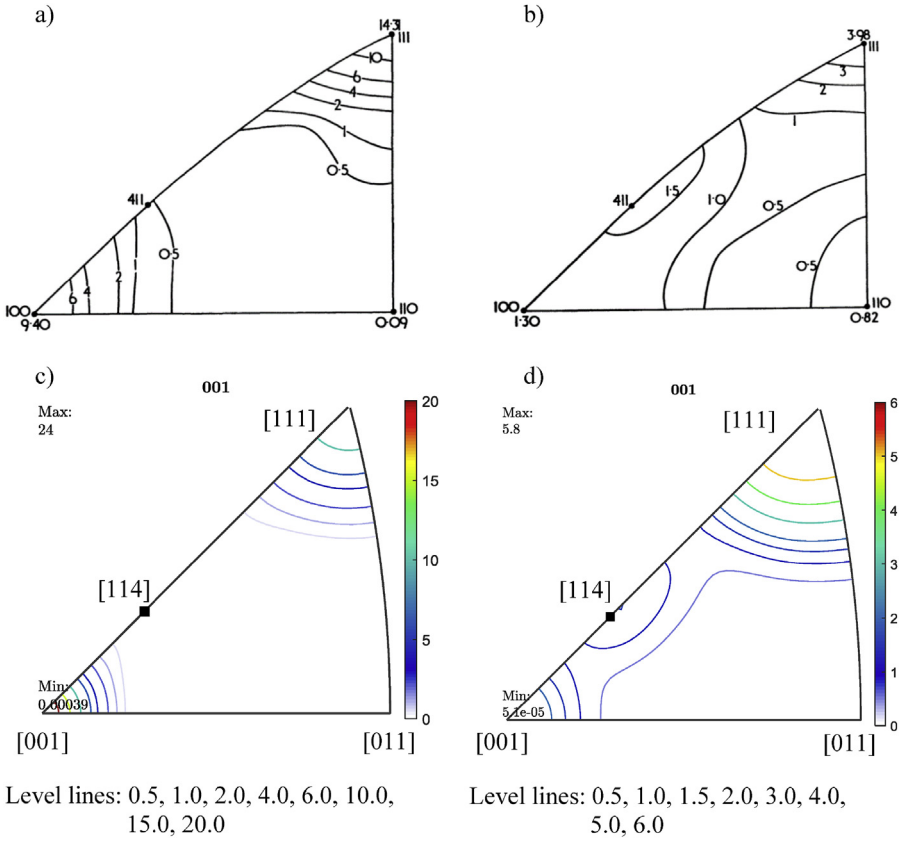

Fig. 8. Inverse pole figures showing deformation and recrystallization textures of 88% compressed iron: a) measured deformation texture; b) measured recrystallized texture; c) predicted deformation texture; d) predicted recrystallized texture.

during tension of fcc polycrystals. For the same applied boundary conditions, the reorientation caused by {110}⟨111⟩ slip in bcc materials has the same magnitude as the reorientation caused by {111}⟨110⟩ slip in fcc materials but in the opposite direction. Consequently, tension of an fcc polycrystal and compression of a bcc polycrystal result in very similar reorientations, if only {111}⟨110⟩ and {110}⟨111⟩ slip are considered, respectively [76]. Similar to the case of tension of copper, the model over-predicts the intensity of the [001] component because the misorientation spreads in the [001] region are under-predicted. The total weights of orientations with compression direction within 15° of [001] and [111] are 0.35 and 0.6, respectively.

Fig. 8b and d shows measured and predicted recrystallization textures. The major [111] and minor [001] components present in

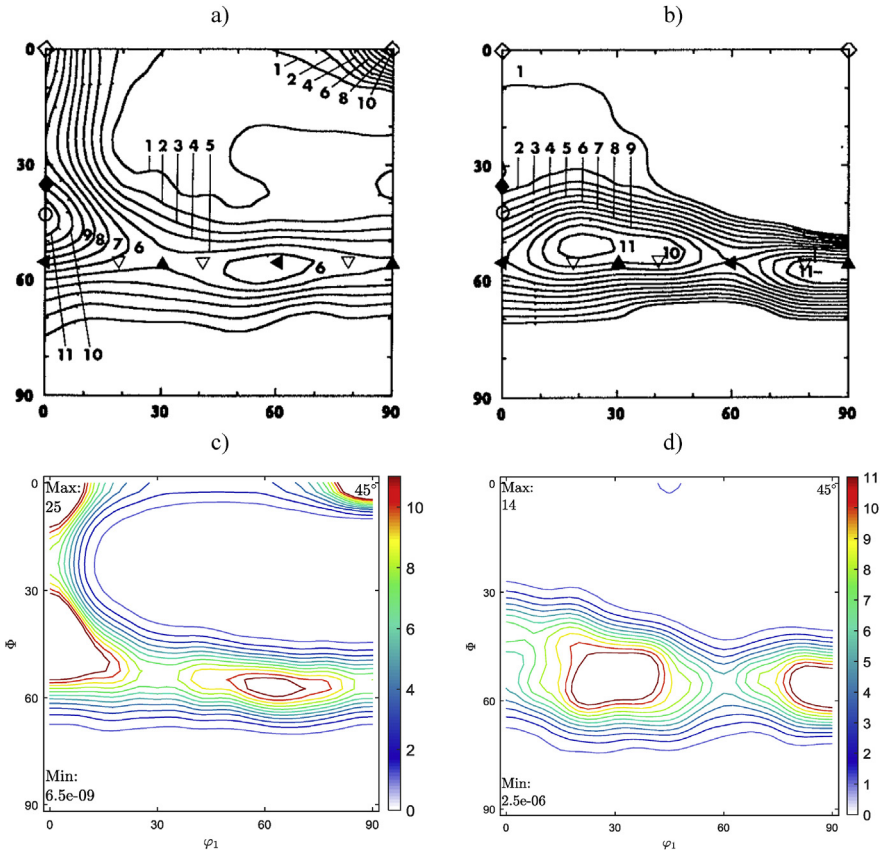

Fig. 9. $\varphi_2 = 45^\circ$ ODF section of deformation and recrystallization textures of 85% rolled IF steel: a) measured deformation texture; b) measured recrystallized texture; c) predicted deformation texture; d) predicted recrystallized texture.

the deformation texture are also present in the measured recrystallization texture. In addition, the [114] and the weak [011] components, which are nearly absent in the deformation texture, emerge during recrystallization. Both components are attributed to transition band nucleation. Orientations on the [114]-[110] line tend to develop transition bands because portions of grains' orientation spreads above the [114]-[110] line converge to the [111] stable component while the portions of grains' orientation spreads below this line converge to [001] stable component [10,76,82]. The transition band orientations consequently converge toward the [114] component. In the predicted recrystallization texture, the [111] and [001] components are formed by the grain boundary nucleation mechanism, while the [114] component is a consequence of the transition band nucleation [52]. Parameters for the recrystallization model are given in Table 1. The [011] component is absent from the predicted recrystallization texture because only a few grains developed transition bands with these orientations. At lower strain (50% compression) the majority of predicted transition band orientations would be in the [011] region. During further straining to 88% compression these transition bands converge to the [114] component.

3.4. Annealing of 85% rolled Ti-Nb IF steel

Rolling and recrystallization of 85% rolled Ti-Nb IF steel is simulated and the predicted textures are compared with experimental measurements [83,84]. We represent the initial texture with 400 randomly oriented spherical grains deforming by $\{110\}\langle 111\rangle$ and $\{112\}\langle 111\rangle$ and linear hardening (Eq. (4)). Initial slip resistance and hardening parameters are assumed to be the same for each mode.

Fig. 9a and c shows the $\varphi_2 = 45^\circ$ section of Euler space for the measured and predicted rolling textures [83,84]. A majority of grains in the experimental texture are concentrated around the γ-fiber and a portion of the α-fiber [66,85,86]. Note that the intensities of these two fibers have been reduced due to the ghost correction applied to the experimental data [83]. The predicted texture qualitatively matches the experimental results, but it is considerably sharper than the measured texture. Again, the likely reason for the discrepancy in intensities is the under-prediction of misorientation spreads of grains in the stable region.

The $\varphi_2 = 45^\circ$ section of Euler space for the measured and predicted recrystallization textures are given on Fig. 9b and d. Comparison of the measured recrystallization texture with the deformation texture indicates that the γ-fiber strengthens during recrystallization, while the α- fiber weakens [66,86–88]. The grains on the γ-fiber possess higher stored energy and are thus favorable nucleation sites [88,89]. The nuclei are commonly observed in the vicinity of grain boundaries [84,90]. Inokuti and Doherty showed that intragranular nucleation at transition bands occurs only sporadically as opposed to the nucleation in compressed iron where a majority of the nuclei formed at the transition bands [10,91]. Considering the experimental observations, in the setup of the recrystallization model, only grain boundary nucleation was allowed in the grains with the highest stored energy (Table 1). The predicted recrystallization texture agrees well with the

experimental texture, and the model corroborates the experimental observations.

4. Conclusions

We developed a coupled deformation and recrystallization model that utilizes intragranular orientation distributions and strain energy fields predicted by the GF-VPSC model. The new formulation incorporates nucleation at grain boundaries and transition bands. The fitting parameters of the recrystallization model are determined based on experimental observations to appropriately weight the probability of nucleation events. Deformation and recrystallization textures of fcc and bcc materials were simulated and reasonable agreement with experiments was achieved. It was found that nucleation at transition bands is responsible for development of the recrystallization texture components that are largely absent from deformation textures. A drastic example is recrystallization of 95% rolled copper, where the strong cube recrystallization texture was found to be predominantly a consequence of transition band nucleation, which is in good agreement with experimental observations. Furthermore, transition band nucleation was also found to be the cause of the [114] recrystallization texture component of compressed iron and the [112] recrystallization texture component of drawn copper wire. On the other hand, the recrystallization texture of rolled IF steel was found to be caused by grain boundary nucleation occurring in grains with highest strain energy, which is experimentally observed. The main deformation texture components were predicted well, but the sharpness of certain components was either under- or over-predicted. The likely reason is the inaccurate evolution of intragranular orientation spreads around those components caused by the inherent limitations of the present mean-field modeling approach.

Acknowledgments

This research was sponsored by the U.S. National Science Foundation under the CAREER grant no. CMMI-1650641 (MK) and Los Alamos National Laboratory (LANL) Directed Research and Development (LDRD) project 20180441ER (RAL and MZ). MZ also acknowledges the financial support provided by the University of New Hampshire Dissertation Year Fellowship program. The contributions of RJM were supported by LANL's LDRD project 20140630ER.

Appendix

Orientations of nuclei originating at grain boundaries

The Cholesky decomposition of the second moment of the grain's misorientation spread is $\langle \delta\mathbf{r} \otimes \delta\mathbf{r} \rangle^{(r)} = \mathbf{L}\mathbf{L}^T$. The lower triangular matrix $\mathbf{L}$ transforms random vectors, $\mathbf{x}$, with zero mean and unit variance to random vectors, $\delta\mathbf{r}^{(r),rand}$, with zero mean and second moment $\langle \delta\mathbf{r} \otimes \delta\mathbf{r} \rangle^{(r)}$:

$$\delta\mathbf{r}^{(r),rand} = \mathbf{L}\mathbf{x}. \tag{A1}$$

Therefore, the inverse matrix, $\mathbf{L}^{-1}$, transforms random vectors $\delta\mathbf{r}^{(r),rand}$ to random vectors $\mathbf{x}$.

In the model, the orientation of a grain boundary nucleus is randomly chosen using a rejection method. First, the distribution of misorientation vectors $\delta\mathbf{r}$ is assumed to be multivariate Gaussian and a random misorientation vector, $\delta\mathbf{r}^{(r),rand}$, is sampled from the grain's misorientation distribution. The sampled random misorientation vector, $\delta\mathbf{r}^{(r),rand}$, is mapped to the random vector, $\mathbf{x}$, with zero mean and unit variance using the matrix $\mathbf{L}^{-1}$. If the length of the vector $\mathbf{x}$ is larger than the constant c, then the length of the vector $\delta\mathbf{r}^{(r),rand}$ is larger than $c \times SD(\delta\mathbf{r}^{(r),rand} / \left|\delta\mathbf{r}^{(r),rand}\right|)$ and the vector $\delta\mathbf{r}^{(r),rand}$ is accepted. $SD(\delta\mathbf{r}^{(r),rand} / \left|\delta\mathbf{r}^{(r),rand}\right|)$ is the standard deviation along the direction of the vector $\delta\mathbf{r}^{(r),rand}$. The constant c defines the magnitude of misorientation of grain boundary orientation with respect to the mean orientation of the grain. If the length of the vector $\mathbf{x}$ is smaller than c, the random vector $\delta\mathbf{r}^{(r),rand}$ is rejected and a new random vector is sampled. The orientation of the nucleus is obtained by composing the randomly sampled misorientation and the mean orientation of the grain.

Orientations of nuclei originating at transition bands

Transition band orientations correspond to orientations in the region between the modes of the bi-modal orientation distribution. The transition band region of the misorientation spread can be identified by the projections of the misorientation vectors to the dominant rotation axis. For transition band regions, these projections have to belong to an interval between the modes of a probability density function (pdf) along the dominant rotation axis. The orientation of the transition band nucleus is randomly sampled from the transition band region using the rejection method. A random misorientation vector, $\delta\mathbf{r}^{(r),rand}$, is sampled from the grain's misorientation distribution and then projected to the dominant rotation axis, $\mathbf{v}^{1,(r)}$. If the projection $\delta\mathbf{r}^{(r),rand} \cdot \mathbf{v}^{1,(r)}$ does not belong to the defined transition band region, a new random misorientation vector is sampled from the spread until the transition band misorientation vector is sampled. The orientation of the nucleus is obtained by composing the randomly sampled misorientation and the mean orientation of the grain.

References

[1] F. Humphreys, M. Hatherly, Recrystallization and Related Annealing Phenomena, Elsevier, 2004.
[2] B. Verlinden, J. Driver, I. Samajdar, R.D. Doherty, Thermo-mechanical Processing of Metallic Materials, Elsevier, 2007.
[3] P.A. Beck, P.R. Sperry, Strain induced grain boundary migration in high purity aluminum, J. Appl. Phys. 21 (1950) 150–152.
[4] G. Gottstein, L.S. Shvindlerman, Grain Boundary Migration in Metals: Thermodynamics, Kinetics, Applications, CRC press, 2009.
[5] H. Hu, Recrystallization by Subgrain Coalescence, Electron Microscopy and Strength of Crystals, Interscience, New York, 1963, pp. 564–573.
[6] J. Walter, E. Koch, Substructures and recrystallization of deformed (100)[001]-oriented crystals of high-purity silicon-iron, Acta Metall. 11 (1963) 923–938.
[7] I. Dillamore, P. Morris, C. Smith, W. Hutchinson, Transition bands and recrystallization in metals, Proc. R. Soc. Lond. A 329 (1972) 405–420.
[8] S.P. Bellier, R.D. Doherty, The structure of deformed aluminum and its recrystallization–investigations with transmission Kossel diffraction, Acta Metall. Mater. 25 (1977) 521–538.
[9] J. Hjelen, R. Ørsund, E. Nes, On the origin of recrystallization textures in aluminium, Acta Metall. Mater. 39 (1991) 1377–1404.
[10] Y. Inokuti, R. Doherty, Transmission Kossel study of the structure of compressed iron and its recrystallization behaviour, Acta Metall. 26 (1978) 61–80.
[11] A. Ridha, W. Hutchinson, Recrystallisation mechanisms and the origin of cube texture in copper, Acta Metall. 30 (1982) 1929–1939.
[12] F. Adcock, The internal mechanism of cold-work and recrystallization in Cupro-Nickel, J. Inst. Met. 27 (1922) 73–92.
[13] B. Duggan, M. Hatherly, W. Hutchinson, P. Wakefield, Deformation structures and textures in cold-rolled 70: 30 brass, Met. Sci. 12 (1978) 343–351.
[14] T. Haratani, W. Hutchinson, I. Dillamore, P. Bate, Contribution of shear banding to origin of Goss texture in silicon iron, Met. Sci. 18 (1984) 57–66.
[15] M. Ardeljan, M. Knezevic, T. Nizolek, I.J. Beyerlein, N.A. Mara, T.M. Pollock, A study of microstructure-driven strain localizations in two-phase polycrystalline HCP/BCC composites using a multi-scale model, Int. J. Plast. 74 (2015) 35–57.
[16] R.A. Lebensohn, R. Brenner, O. Castelnau, A.D. Rollett, Orientation image-based micromechanical modelling of subgrain texture evolution in polycrystalline copper, Acta Mater. 56 (2008) 3914–3926.

[17] R.A. Lebensohn, N-site modeling of a 3D viscoplastic polycrystal using fast Fourier transform, Acta Mater. 49 (2001) 2723–2737.
[18] S.R. Kalidindi, C.A. Bronkhorst, L. Anand, Crystallographic texture evolution in bulk deformation processing of FCC metals, J. Mech. Phys. Solid. 40 (1992) 537–569.
[19] M. Knezevic, B. Drach, M. Ardeljan, I.J. Beyerlein, Three dimensional predictions of grain scale plasticity and grain boundaries using crystal plasticity finite element models, Comput. Methods Appl. Mech. Eng. 277 (2014) 239–259.
[20] M. Ardeljan, I.J. Beyerlein, M. Knezevic, A dislocation density based crystal plasticity finite element model: application to a two-phase polycrystalline HCP/BCC composites, J. Mech. Phys. Solid. 66 (2014) 16–31.
[21] M. Knezevic, J. Crapps, I.J. Beyerlein, D.R. Coughlin, K.D. Clarke, R.J. McCabe, Anisotropic modeling of structural components using embedded crystal plasticity constructive laws within finite elements, Int. J. Mech. Sci. 105 (2016) 227–238.
[22] M. Ardeljan, M. Knezevic, Explicit modeling of double twinning in AZ31 using crystal plasticity finite elements for predicting the mechanical fields for twin variant selection and fracture analyses, Acta Mater. 157 (2018) 339–354.
[23] D.J. Srolovitz, M.P. Anderson, P.S. Sahni, G.S. Grest, Computer-simulation of grain-growth .2. Grain-size distribution, topology, and local dynamics, Acta Metall. 32 (1984) 793–802.
[24] D.J. Srolovitz, M.P. Anderson, G.S. Grest, P.S. Sahni, Computer-simulation of grain-growth .3. Influence of a particle dispersion, Acta Metall. 32 (1984) 1429–1438.
[25] M.P. Anderson, D.J. Srolovitz, G.S. Grest, P.S. Sahni, Computer-simulation of grain-growth .1. Kinetics, Acta Metall. 32 (1984) 783–791.
[26] A. Rollett, Overview of modeling and simulation of recrystallization, Prog. Mater. Sci. 42 (1997) 79–99.
[27] M.A. Steiner, R.J. McCabe, E. Garlea, S.R. Agnew, Monte Carlo modeling of recrystallization processes in α-uranium, J. Nucl. Mater. 492 (2017) 74–87.
[28] D. Raabe, Cellular automata in materials science with particular reference to recrystallization simulation, Annu. Rev. Mater. Res. 32 (2002) 53–76.
[29] D. Raabe, Introduction of a scalable three-dimensional cellular automaton with a probabilistic switching rule for the discrete mesoscale simulation of recrystallization phenomena, Philos. Mag. A 79 (1999) 2339–2358.
[30] H. Hallberg, Approaches to modeling of recrystallization, Metals 1 (2011) 16–48.
[31] A. Molinari, G.R. Canova, S. Ahzi, Self consistent approach of the large deformation polycrystal viscoplasticity, Acta Metall. Mater. 35 (1987) 2983–2994.
[32] R.A. Lebensohn, C.N. Tomé, A self-consistent anisotropic approach for the simulation of plastic deformation and texture development of polycrystals: application to zirconium alloys, Acta Metall. Mater. 41 (1993) 2611–2624.
[33] J.W. Hutchinson, Proc. Roy. Soc. Lond. A319 (1970) 247.
[34] M. Zecevic, M. Knezevic, A dislocation density based elasto-plastic self-consistent model for the prediction of cyclic deformation: application to Al6022-T4, Int. J. Plast. 72 (2015) 200–217.
[35] M. Zecevic, M. Knezevic, Latent hardening within the elasto-plastic self-consistent polycrystal homogenization to enable the prediction of anisotropy of AA6022-T4 sheets, Int. J. Plast. 105 (2018) 141–163.
[36] H. Bunge, U. Köhler, Model calculations of primary recrystallization textures, Scripta Metall. Mater. 27 (1992) 1539–1543.
[37] O. Engler, A simulation of recrystallization textures of Al-alloys with consideration of the probabilities of nucleation and growth, Texture, Stress, Microstruct. 32 (1999) 197–219.
[38] L. Kestens, J. Jonas, Modeling texture change during the static recrystallization of interstitial free steels, Metall. Mater. Trans. 27 (1996) 155–164.
[39] C. Tomé, R.A. Lebensohn, U. Kocks, A model for texture development dominated by deformation twinning: application to zirconium alloys, Acta Metall. Mater. 39 (1991) 2667–2680.
[40] A. Hildenbrand, L. Tóth, A. Molinari, J. Baczynski, J. Jonas, Self-consistent polycrystal modelling of dynamic recrystallization during the shear deformation of a Ti IF steel, Acta Mater. 47 (1999) 447–460.
[41] H.-R. Wenk, G. Canova, Y. Brechet, L. Flandin, A deformation-based model for recrystallization of anisotropic materials, Acta Mater. 45 (1997) 3283–3296.
[42] R. Lebensohn, H.-R. Wenk, C. Tomé, Modelling deformation and recrystallization textures in calcite, Acta Mater. 46 (1998) 2683–2693.
[43] H.R. Wenk, C. Tomé, Modeling dynamic recrystallization of olivine aggregates deformed in simple shear, J. Geophys. Res.: Solid Earth 104 (1999) 25513–25527.
[44] R.E. Bolmaro, A. Roatta, A.L. Fourty, J.W. Signorelli, Recrystallization textures in fcc materials: a simulation based on micromechanical modeling data, Scripta Mater. 53 (2005) 147–152.
[45] O. Bouaziz, P. Buessler, Iso-work increment assumption for heterogeneous material behaviour modelling, Adv. Eng. Mater. 6 (2004) 79–83.
[46] H. Zurob, Y. Brechet, J. Dunlop, Quantitative criterion for recrystallization nucleation in single-phase alloys: prediction of critical strains and incubation times, Acta Mater. 54 (2006) 3983–3990.
[47] D. Cram, H. Zurob, Y. Brechet, C. Hutchinson, Modelling discontinuous dynamic recrystallization using a physically based model for nucleation, Acta Mater. 57 (2009) 5218–5228.
[48] F. Humphreys, A unified theory of recovery, recrystallization and grain growth, based on the stability and growth of cellular microstructures—II. The effect of second-phase particles, Acta Mater. 45 (1997) 5031–5039.
[49] F. Han, B. Tang, H. Kou, L. Cheng, J. Li, Y. Feng, Static recrystallization simulations by coupling cellular automata and crystal plasticity finite element method using a physically based model for nucleation, J. Mater. Sci. 49 (2014) 3253–3267.
[50] R. Sebald, G. Gottstein, Modeling of recrystallization textures: interaction of nucleation and growth, Acta Mater. 50 (2002) 1587–1598.
[51] M. Zecevic, W. Pantleon, R.A. Lebensohn, R.J. McCabe, M. Knezevic, Predicting intragranular misorientation distributions in polycrystalline metals using the viscoplastic self-consistent formulation, Acta Mater. 140 (2017) 398–410.
[52] R.A. Lebensohn, M. Zecevic, M. Knezevic, R.J. McCabe, Average intragranular misorientation trends in polycrystalline materials predicted by a viscoplastic self-consistent approach, Acta Mater. 104 (2016) 228–236.
[53] M. Zecevic, R.A. Lebensohn, R.J. McCabe, M. Knezevic, Modeling of Intragranular Misorientation and Grain Fragmentation in Polycrystalline Materials Using the Viscoplastic Self-consistent Formulation International Journal of Plasticity, 2018.
[54] R.A. Lebensohn, C.N. Tome, P.P. Castaneda, Self-consistent modelling of the mechanical behaviour of viscoplastic polycrystals incorporating intragranular field fluctuations, Phil. Mag. 87 (2007) 4287–4322.
[55] R. Masson, M. Bornert, P. Suquet, A. Zaoui, An affine formulation for the prediction of the effective properties of nonlinear composites and polycrystals, J. Mech. Phys. Solid. 48 (2000) 1203–1227.
[56] J.D. Eshelby, The determination of the elastic field of an ellipsoidal inclusion, and related problems, Proc R. Soc. Lond. A 241 (1957) 376–396.
[57] O. Castelnau, R. Brenner, R. Lebensohn, The effect of strain heterogeneity on the work hardening of polycrystals predicted by mean-field approaches, Acta Mater. 54 (2006) 2745–2756.
[58] M. Bobeth, G. Diener, Field fluctuations in multicomponent mixtures, J. Mech. Phys. Solid. 34 (1986) 1–17.
[59] R.A. Lebensohn, Y. Liu, P.P. Castaneda, On the accuracy of the self-consistent approximation for polycrystals: comparison with full-field numerical simulations, Acta Mater. 52 (2004) 5347–5361.
[60] M. Bobeth, G. Diener, Static elastic and thermoelastic field fluctuations in multiphase composites, J. Mech. Phys. Solid. 35 (1987) 137–149.
[61] W. Kreher, Residual stresses and stored elastic energy of composites and polycrystals, J. Mech. Phys. Solid. 38 (1990) 115–128.
[62] R. Doherty, D. Hughes, F. Humphreys, J. Jonas, D.J. Jensen, M. Kassner, W. King, T. McNelley, H. McQueen, A. Rollett, Current issues in recrystallization: a review, Mater. Sci. Eng., A 238 (1997) 219–274.
[63] O. Engler, Nucleation and growth during recrystallisation of aluminium alloys investigated by local texture analysis, Mater. Sci. Technol. 12 (1996) 859–872.
[64] P. Bromiley, Products and convolutions of Gaussian probability density functions, Tina-Vision Memo 3 (2003) 1.
[65] J. Pospiech, K. Lücke, K. Sztwiertnia, Orientation distribution and orientation correlation functions for description of microstructures, Acta Metall. Mater. 41 (1993) 305–321.
[66] V. Randle, O. Engler, Introduction to texture analysis, in: Macrotexture, Microstructure & Orientation Mapping, Gordon and Breach Science Publishers, 2000.
[67] M.V. Sadovskii, Statistical Physics, Volume 18 of De Gruyter Studies in Mathematical Physics, first ed., Walter de Gruyter, Berlin, Germany, 2012, p. 292.
[68] A. Papoulis, Probability, Random Variables and Stochastic Processes, McGraw-Hill, Inc., New York, 1991.
[69] D. Hughes, N. Hansen, High angle boundaries formed by grain subdivision mechanisms, Acta Mater. 45 (1997) 3871–3886.
[70] W. Pantleon, N. Hansen, Dislocation boundaries—the distribution function of disorientation angles, Acta Mater. 49 (2001) 1479–1493.
[71] D. Hull, D.J. Bacon, Introduction to Dislocations, Butterworth-Heinemann, 2001.
[72] J.P. Hirth, J. Lothe, Theory of Dislocations, second ed., Krieger Pub. Co, Malabar, FL, USA, 1982, p. 839.
[73] S. Mishra, P. Pant, K. Narasimhan, A. Rollett, I. Samajdar, On the widths of orientation gradient zones adjacent to grain boundaries, Scripta Mater. 61 (2009) 273–276.
[74] R.J. McCabe, A.W. Richards, D.R. Coughlin, K.D. Clarke, I.J. Beyerlein, M. Knezevic, Microstructure effects on the recrystallization of low-symmetry alpha-uranium, J. Nucl. Mater. 465 (2015) 189–195.
[75] N. Hansen, D.J. Jensen, Development of microstructure in FCC metals during cold work, Phil. Trans. Roy. Soc. Lond.: Math. Phys. Eng. Sci. 357 (1999) 1447–1469.
[76] I. Dillamore, H. Katoh, Mechanisms of recrystallization in cubic metals with particular reference to their orientation-dependence, Met. Sci. 8 (1974) 73–83.
[77] W. Pantleon, Retrieving orientation correlations in deformation structures from orientation maps, Mater. Sci. Technol. 21 (2005) 1392–1396.
[78] H. Park, D.N. Lee, The evolution of annealing textures in 90 pct drawn copper wire, Metall. Mater. Trans. 34 (2003) 531.
[79] A. English, G. Chin, On the variation of wire texture with stacking fault energy in fcc metals and alloys, Acta Metall. 13 (1965) 1013–1016.
[80] K. Rajan, R. Petkie, Microtexture and anisotropy in wire drawn copper, Mater. Sci. Eng., A 257 (1998) 185–197.
[81] I. Dillamore, Factors affecting the rolling recrystallisation textures in FCC metals, Acta Metall. 12 (1964) 1005–1014.
[82] I. Dillamore, H. Katoh, K. Haslam, The nucleation of recrystallisation and the development of textures in heavily compressed iron-carbon alloys, Texture,

Stress, Microstruct. 1 (1974) 151–156.
[83] T. Urabe, J.J. Jonas, Modeling texture change during the recrystallization of an IF steel, ISIJ Int. 34 (1994) 435–442.
[84] R. Ray, J.J. Jonas, R. Hook, Cold rolling and annealing textures in low carbon and extra low carbon steels, Int. Mater. Rev. 39 (1994) 129–172.
[85] U. Von Schlippenbach, F. Emren, K. Lücke, Investigation of the development of the cold rolling texture in deep drawing steels by ODF-analysis, Acta Metall. 34 (1986) 1289–1301.
[86] K. Lücke, M. Hölscher, Rolling and recrystallization textures of BCC steels, Texture, Stress, Microstruct. 14 (1991) 585–596.
[87] F. Emren, U. Von Schlippenbach, K. Lücke, Investigation of the development of the recrystallization textures in deep drawing steels by ODF analysis, Acta Metall. 34 (1986) 2105–2117.
[88] I. Samajdar, B. Verlinden, P. Van Houtte, D. Vanderschueren, γ-Fibre recrystallization texture in IF-steel: an investigation on the recrystallization mechanisms, Mater. Sci. Eng., A 238 (1997) 343–350.
[89] N. Rajmohan, Y. Hayakawa, J. Szpunar, J. Root, Neutron diffraction method for stored energy measurement in interstitial free steel, Acta Mater. 45 (1997) 2485–2494.
[90] W. Hutchinson, Recrystallisation textures in iron resulting from nucleation at grain boundaries, Acta Metall. 37 (1989) 1047–1056.
[91] Y. Inokuti, R. Doherty, Transmission Kossel study of the structure of cold-rolled iron and its nucleation behaviour, Texture, Stress, Microstruct. 2 (1977) 143–168.